Article

Cell Metabolism

mTORC1 Inactivation Promotes Colitis-Induced Colorectal Cancer but Protects from APC Loss-Dependent Tumorigenesis

Graphical Abstract

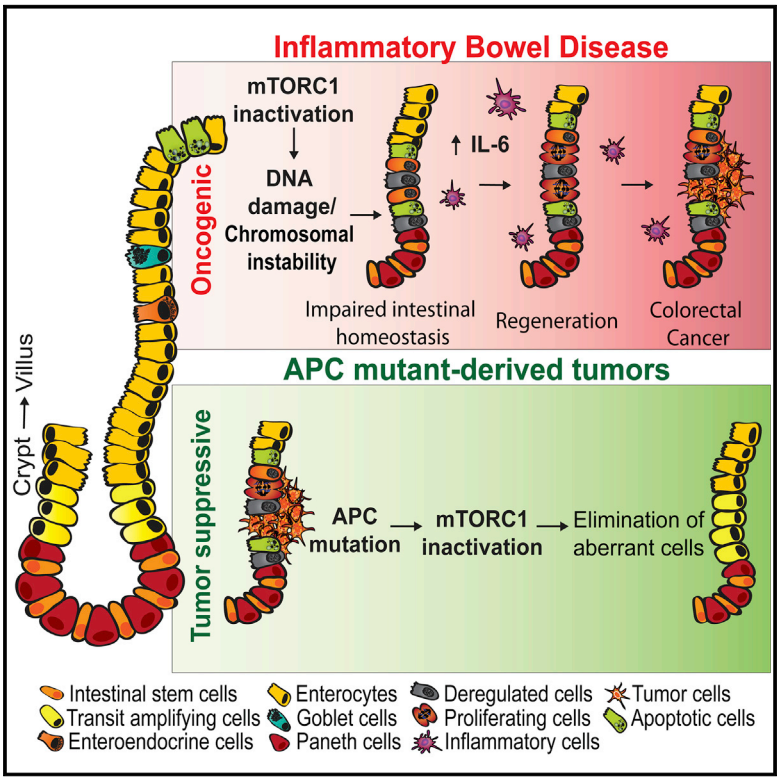

Highlights

- mTORC1 activity is important for intestinal tissue homeostasis and regeneration
- mTORC1 inactivation-induced DNA damage and CIN trigger IL-6 -dependent CRC
- mTORC1 inactivation reduces tumor incidence in mouse models with APC inactivation
- mTORC1 inactivation correlates with inflammation in colitis-induced CRC patients

Authors

Marta Brandt, Tatiana P. Grazioso, Mohamad-Ali Fawal, ..., Sandra Rodriguez-Perales, Cristian Perna, Nabil Djouder

Correspondence

ndjouder@cnio.es

In Brief

Brandt et al. shed light on the mechanisms linking nutrients, inflammation, and colorectal cancer (CRC) and show that mTORC1 inactivation promotes CRC in a colitis mouse model, but reduces tumorigenesis in mice with APC inactivation, demonstrating mTORC1's oncogenic and tumor-suppressive roles in the intestinal epithelium.

Brandt et al., 2018, Cell Metabolism 27, 118–135
January 9, 2018
https://doi.org/10.1016/j.cmet.2017.11.006

CellPress

CellPress

Cell Metabolism
Article

mTORC1 Inactivation Promotes Colitis-Induced Colorectal Cancer but Protects from APC Loss-Dependent Tumorigenesis

Marta Brandt,[1] Tatiana P. Grazioso,[1] Mohamad-Ali Fawal,[1] Krishna S. Tummala,[1] Raul Torres-Ruiz,[2] Sandra Rodriguez-Perales,[2] Cristian Perna,[3] and Nabil Djouder[1,4,*]
[1]Cancer Cell Biology Programme, Growth Factors, Nutrients and Cancer Group
[2]Molecular Cytogenetics Unit
Centro Nacional de Investigaciones Oncológicas, CNIO, Madrid 28029, Spain
[3]Department of Pathology, Hospital Universitario Ramón y Cajal, IRYCIS, Madrid 28034, Spain
[4]Lead Contact
*Correspondence: ndjouder@cnio.es
https://doi.org/10.1016/j.cmet.2017.11.006

SUMMARY

Dietary habits that can induce inflammatory bowel disease (IBD) are major colorectal cancer (CRC) risk factors, but mechanisms linking nutrients, IBD, and CRC are unknown. Using human data and mouse models, we show that mTORC1 inactivation-induced chromosomal instability impairs intestinal crypt proliferation and regeneration, CDK4/6 dependently. This triggers interleukin (IL)-6-associated reparative inflammation, inducing crypt hyper-proliferation, wound healing, and CRC. Blocking IL-6 signaling or reactivating mTORC1 reduces inflammation-induced CRC, so mTORC1 activation suppresses tumorigenesis in IBD. Conversely, mTORC1 inactivation is beneficial in APC loss-dependent CRC. Thus, IL-6 blockers or protein-rich-diet-linked mTORC1 activation may prevent IBD-associated CRC. However, abolishing mTORC1 can mitigate CRC in predisposed patients with *APC* mutations. Our work reveals mTORC1 oncogenic and tumor-suppressive roles in intestinal epithelium and avenues to optimized and personalized therapeutic regimens for CRC.

INTRODUCTION

Colon or colorectal cancer (CRC) is common, frequently resistant to conventional therapies, and often lethal (Brenner et al., 2014). Hereditary CRC, accounting for about 5% of cases, is mainly linked to several familial CRC syndromes. These include hereditary non-polyposis CRC and familial adenomatous polyposis (FAP), caused by *APC* mutations, leading to β-catenin stabilization and activation (Brenner et al., 2014). FAP patients develop numerous colonic polyps early in life, usually followed by CRC.

However, most risk factors are related to Western lifestyles (>75% of CRC patients have few or no genetic risk factors). Environmental factors, including poor diet and lack of physical activity, may impair enteric function, metabolism, and energy balances, potentially leading to intestinal diseases such as inflammatory bowel disease (IBD), a chronic intestinal inflammation encompassing ulcerative colitis (UC) and Crohn disease (CD) that can progress to CRC (Brenner et al., 2014). Without genetic risk factors, *APC* mutations may not occur at early stages of tumor progression, and thus are not leading causes of tumorigenesis, but poor-diet-associated inflammation may drive CRC via unknown mechanisms.

The mammalian/mechanistic target of rapamycin complex 1 (mTORC1) plays key roles in integrating nutrient signals and has putative oncogenic activities. It is deregulated in IBD, and its activation in human CRC is linked to poor prognosis (Francipane and Lagasse, 2014; Gulhati et al., 2009; Zhang et al., 2009). The small guanosine triphosphatase Rab1A activating mTORC1 and microspherule protein 1 (MCRS1) linking nutrient surpluses to mTORC1 activation is also overexpressed in CRC and correlated with poor prognosis (Fawal et al., 2015; Thomas et al., 2014). Further, mTORC1 inactivation reduces growth of APC-deficient adenomas by inhibiting translational elongation (Faller et al., 2015). This suggests an oncogenic role of mTORC1 in CRC, mainly in patients with *APC* mutations. Thus, mTORC1 inhibitors (rapalogs) have emerged as potential CRC therapeutics (Liko and Hall, 2015), but solid tumor responses to rapalogs are modest (Wang and Zhang, 2014). Better understanding of mTORC1's roles in intestinal disorders and CRC is needed to develop optimal personalized therapeutic regimens.

The intestinal lining's rapid renewal is regulated by balanced proliferation, differentiation, and apoptosis of intestinal stem cells (ISCs) in the crypts of Lieberkühn (Clevers, 2013). The mTORC1 pathway participates in intestinal regeneration (Yang et al., 2015), and mTORC1 inhibition may lead to non-cell-autonomous increases in ISC self-renewal (Yilmaz et al., 2012). mTORC1 also has key regulatory roles in anabolic metabolism, cellular growth, proliferation, and survival in accordance with nutrient availability (Bar-Peled and Sabatini, 2014; Djouder et al., 2007; Dowling et al., 2010; Montagne et al., 1999). In addition, following mTORC1/S6K1-mediated

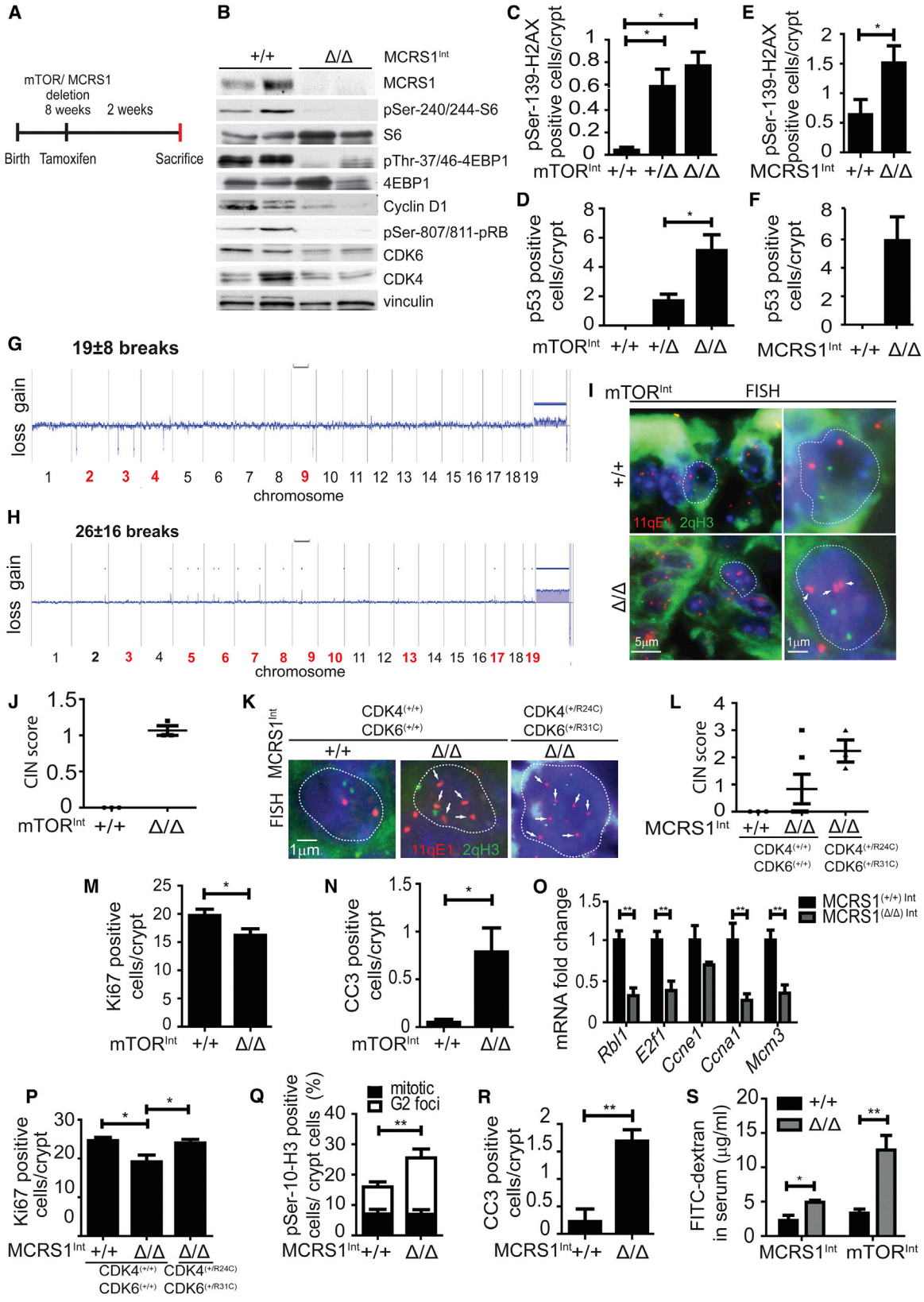

(legend on next page)

phosphorylation, carbamoyl-phosphate synthetase 2 (CAD) catalyzes three steps of the *de novo* pyrimidine synthesis required in deoxynucleotide generation, thereby stimulating essential purine and pyrimidine synthesis during replication (Ben-Sahra et al., 2013, 2016; Robitaille et al., 2013). Thus, mTORC1 inactivation can lead to nucleotide deficiencies, promoting replicative stress, DNA damage, and chromosomal instability (CIN), perturbing intestinal homeostasis (Bester et al., 2011; Burrell et al., 2013). Accordingly, knockdown of MCRS1 in several human cell lines induces p53-dependent aneuploidy (Hsu et al., 2012). Also, deletion of the mTORC1 activating component RagA leads to apoptosis and atrophy in the small intestine (Efeyan et al., 2014). Moreover, Raptor deficiency affects intestinal regeneration (Guan et al., 2015; Sampson et al., 2016) and induces cell-cycle abnormalities associated with instability of cyclin complexes (Hoshii et al., 2014). Finally, mTORC1 repression by rapamycin or genetic haploinsufficiency of Rheb impairs intestinal cell proliferation, induces apoptosis, and inhibits tissue regeneration, leading to high mortality in a murine colitis model (Guan et al., 2015).

Inflammatory modulators also maintain intestinal homeostasis and promote regeneration of injured intestinal tissue through several conserved pathways (Karin and Clevers, 2016). Interleukin (IL)-6 signaling plays a key role, stimulating healing and maintenance of barrier function, by activating gp130 signaling and inducing Src and Yes kinases. This results in stabilization and translocation to the nucleus of Yes-associated protein (YAP), which induces transcription of genes encoding Notch receptors and ligands that enhance ISCs' proliferative capacity (Grivennikov et al., 2009; Taniguchi et al., 2015). Impairment of this inflammatory response may perturb intestinal homeostasis and raise risks of CRC. Weak inflammation may lead to incomplete tissue regeneration, while in IBD, excessive regeneration may lead to disorganization of intestinal architecture and CRC. Hence, IL-6 levels are elevated in mouse CRC models and human CRC patients (Grivennikov et al., 2009). However, mechanisms causing the inflammatory flip to CRC promotion, and linking inflammation to CRC (possibly involving mTORC1 deregulation in early stages), are largely unknown. Analyses of mouse models and human samples presented here indicate mechanisms whereby diet-associated changes in mTORC1 activation contribute to intestinal disorders, providing insights into both oncogenic and tumor-suppressive roles of mTORC1 in CRC.

RESULTS

DNA Damage and CIN Induced by mTORC1 Inactivation Impair Crypt Proliferation and Intestinal Tissue Homeostasis

To confirm involvement of mTOR in intestinal homeostasis, we generated mice in which mTOR could be deleted by tamoxifen treatment by crossing Villin-CreERT2 and $mTOR^{lox/lox}$ mice (el Marjou et al., 2004; Risson et al., 2009) (Figure S1A). We also created mice in which tamoxifen could specifically inhibit mTORC1 via deletion of MCRS1 (which activates mTORC1 in response to amino acids) by crossing Villin-CreERT2 and $MCRS1^{lox/lox}$ mice (Fawal et al., 2015) (Figures S1A and S1B). After 2 weeks of tamoxifen treatment, in intestinal epithelia of the resulting $mTOR^{(\Delta/\Delta)Int}$ mice, we detected reduced mTORC1 signaling, manifested by dephosphorylation of ribosomal protein S6 and eukaryotic translation initiation factor 4E-binding protein 1 (4EBP1) at Ser-240/244 and Thr-37/46, respectively (Figures 1A and S1C). Phosphorylation of CAD at Ser-1859 was also abolished (Figure S1C). Notably, AKT phosphorylation at Ser-473 (a target of mTORC2) was reduced, but AMPK activity was not affected in $mTOR^{(\Delta/\Delta)Int}$ mice (Figures S1C and S1E). The same effects were seen in $MCRS1^{(\Delta/\Delta)Int}$ mice, except that AKT phosphorylation at Ser-473 was slightly increased, possibly due to abrogation of the S6K1-dependent negative feedback loop on IRS1 (Figures 1B, S1D, and S1E).

Both $mTOR^{(\Delta/\Delta)Int}$ and $MCRS1^{(\Delta/\Delta)Int}$ mice showed no differences from their littermate controls in body weight, villi length, crypt architecture, differentiation capacity, numbers of Goblet cells, or WNT/β-catenin target gene expression (Figures S1F and S1G). Further analyses indicated replicative stress and DNA damage responses, manifested by increased phosphorylation of H2AX (γ-H2AX) and p53 in crypt compartments of $mTOR^{(+/\Delta)Int}$, $mTOR^{(\Delta/\Delta)Int}$, and $MCRS1^{(\Delta/\Delta)Int}$ mice (Figures 1C–1F, S1C, and S1D). CIN in intestinal tissue of $mTOR^{(\Delta/\Delta)Int}$ and $MCRS1^{(\Delta/\Delta)Int}$ mice was also detected by array comparative genomic hybridization (aCGH: 19 ± 8 and 26 ± 16 breaks, respectively) and fluorescence *in situ* hybridization (FISH) (CIN scores: 1.07 ± 0.12 and 0.83 ± 1.33, respectively) (Figures 1G–1L), suggesting chromosomal aberrations.

Importantly, reduced crypt cell proliferation and increased apoptosis were detected in $mTOR^{(\Delta/\Delta)Int}$ mouse intestine (Figures 1M, 1N, and S1H). To check dependency of these effects on mTORC1 inactivation, we analyzed intestinal proliferative

Figure 1. DNA Damage and CIN Induced by mTORC1 Inactivation Impair Crypt Proliferation and Intestinal Tissue Homeostasis

(A) Scheme of tamoxifen-treated $mTOR^{Int}$ and $MCRS1^{Int}$ mice.

(B) Western blot from $MCRS1^{Int}$ intestines 2 weeks after MCRS1 deletion.

(C–F) Quantification of pSer-139-H2AX and p53 of intestinal sections from Figures S1C and S1D of $mTOR^{Int}$ (C and D) and $MCRS1^{Int}$ mice (E and F).

(G and H) Representative aCGH from $mTOR^{Int}$ (G) and $MCRS1^{Int}$ (H) intestines 2 weeks after deletion (n = 3). Affected chromosomes are highlighted in bold red.

(I and J) FISH with 11qE1 (red) and 2qH3 (green) probes (I) and quantification of CIN (J) in intestines from $mTOR^{Int}$ mice killed 2 weeks after deletion (n = 3).

(K and L) FISH with 11qE1 (red) and 2qH3 (green) probes (K) from $MCRS1^{(+/+)Int}$ (n = 3), $MCRS1^{(\Delta/\Delta)Int}$ (n = 6) and $MCRS1^{(\Delta/\Delta)Int}$; CDK4(+/KI); CDK6 (+/KI) intestines 2 weeks after MCRS1 deletion, and quantification of CIN (L).

(M and N) Quantification of Ki67 (M) and cleaved caspase-3 (CC3) (N) from Figure S1H in $mTOR^{Int}$ intestines 2 weeks after deletion (n = 4).

(O) qRT-PCR from $MCRS1^{Int}$ intestines 2 weeks after deletion (n = 6).

(P–R) Quantification of Ki67 (P), pSer-10-H3 (Q), and CC3 (R) from Figure S1D in $MCRS1^{Int}$ intestines 2 weeks after deletion.

(S) FITC-dextran in serum from $MCRS1^{Int}$ and $mTOR^{Int}$ mice (n = 3).

Data are represented as means ± SEM; *p ≤ 0.05, **p ≤ 0.01 (Student's t tests); scale bars, 5 μm and 1 μm (I and K); arrowheads indicate CIN (I and K); white dashed line highlights a single nucleus (I and K); at least 50 crypts (C–F, M, N, and P–R) and 100 nuclei (I, J, K, and L) were analyzed in each independent experiment. See also Figure S1 and Table S1.

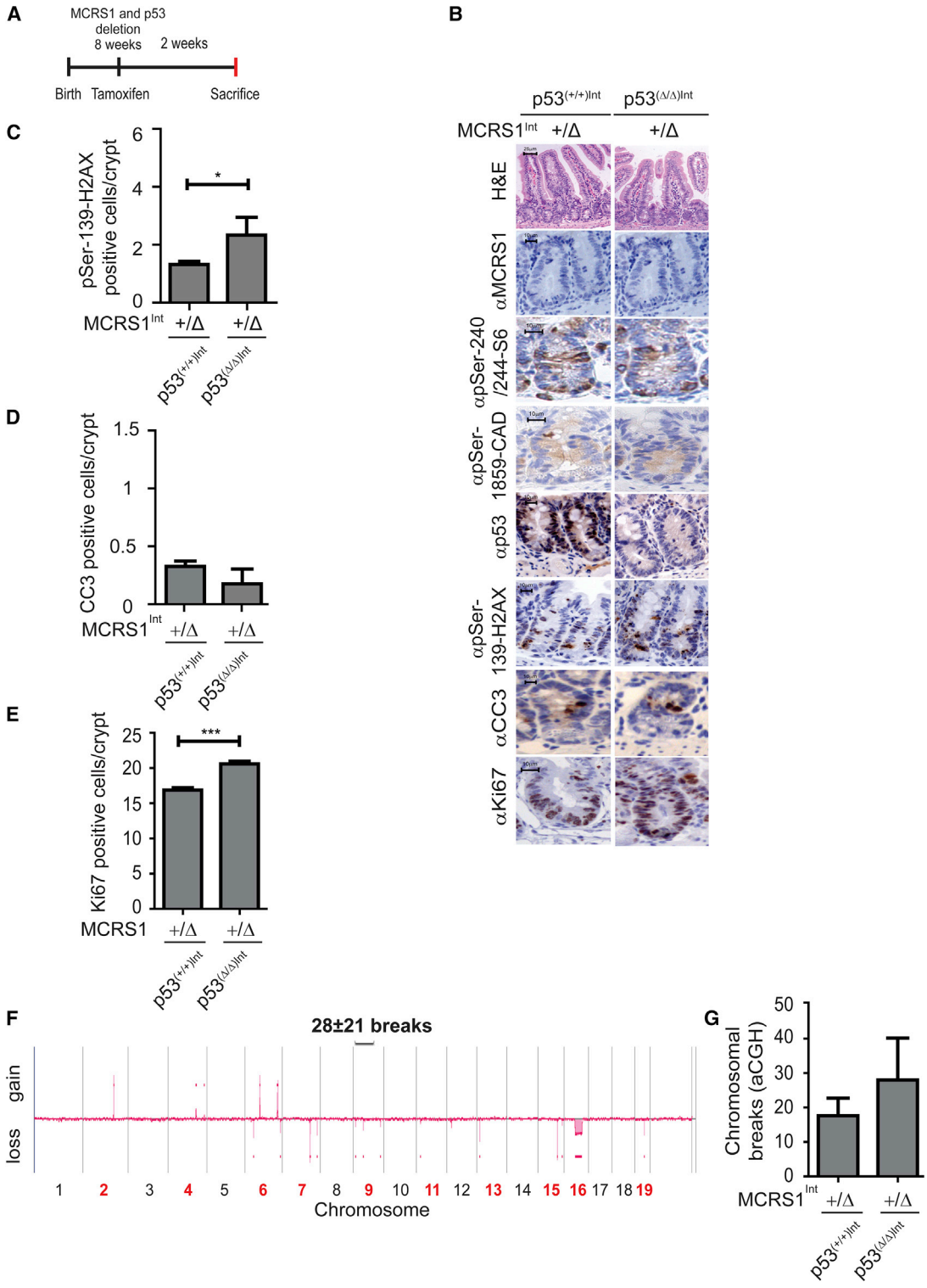

Figure 2. MCRS1 and p53 Deletion Increases DNA Damage and CIN

(A) Scheme of tamoxifen-treated MCRS1^{Int} and MCRS1^{Int}; p53$^{(\Delta/\Delta)Int}$ mice.

(B) H&E and immunohistochemistry (IHC) from MCRS1^{Int} and MCRS1^{Int}; p53$^{(\Delta/\Delta)Int}$ intestines 2 weeks after MCRS1 and p53 deletion (n = 6).

(C and D) Quantification of pSer-139-H2AX (C) and CC3 (D) from (B).

(E) Quantification of Ki67 IHC from MCRS1^{Int} and MCRS1^{Int}; p53$^{(\Delta/\Delta)Int}$ intestines 2 weeks after MCRS1 and p53 deletion (n = 6).

(legend continued on next page)

capacity in MCRS1$^{(\Delta/\Delta)Int}$ mice. Various markers revealed impairment of crypt cell proliferation and the CDK4/CDK6/pRB/E2F pathway in intestines of MCRS1$^{(\Delta/\Delta)Int}$ mice (Figures 1B, 1O, 1P, and S1D), confirming that p53 induction following DNA damage represses CDK4 activity (Ewen et al., 1995; He et al., 2005). In addition, foci-like staining of histone 3 phosphorylation at Ser-10 was enhanced, suggesting blockage of crypt cells in the G2 cell-cycle phase (Figures 1Q and S1D). Moreover, MCRS1$^{(\Delta/\Delta)Int}$ mice had higher levels of cleaved caspase-3 (CC3) in their crypts than their littermates (Figures 1R and S1D), but we detected no senescence, WNT signaling defects, or increases in inflammation in their intestines (Figures S1I–S1K). Furthermore, expressing dominant active kinases CDK4 and CDK6 (Rodriguez-Diez et al., 2014) in MCRS1$^{(\Delta/\Delta)Int}$ mice reinstated intestinal proliferative capacity (Figure 1P) and increased CIN levels (Figures 1K and 1L).

To dissect the order of intestinal processes and events affected by mTORC1 inactivation, we analyzed early stages. After 2 days of tamoxifen treatment (Figure S1L), mTOR$^{(\Delta/\Delta)Int}$ and MCRS1$^{(\Delta/\Delta)Int}$ mice showed impaired mTORC1 signaling (reduced phosphorylation of S6, 4EBP1, and CAD), increased DNA damage, and chromosomal aberrations (FISH scores 1.3 ± 0.1 and 1.3 ± 0.3, respectively, and aCGH scores 89 ± 41 and 11 ± 8) (Figures S1M–S1R). However, proliferation was not affected and apoptosis was increased (Figures S1M, S1N, S1S, and S1T), indicating that DNA damage and CIN precede proliferation defects. Notably, no differences in levels of ATP, reactive oxygen species (ROS), or mtDNA in intestinal tissues of mTOR$^{(\Delta/\Delta)Int}$ or MCRS1$^{(\Delta/\Delta)Int}$ mice (or littermate controls) were detected (Figures S1U and S1V), suggesting that mitochondrial activity and biogenesis in intestinal tissues are not affected by mTORC1 inactivation, and ROS do not contribute to DNA damage/CIN. Thus, mTORC1 inactivation induces DNA damage and CIN, thereby impairing crypt proliferation.

This was confirmed by depleting MCRS1 using specific siRNA in HCT-116 colorectal cells (Fawal et al., 2015), which increased CIN levels (Figure S1W), as previously reported (Hsu et al., 2012). Further, mTORC1 activation was abolished in intestinal tissues by crossing RagA$^{lox/lox}$ and Villin-CreERT2 mice (Efeyan et al., 2014) (Figure S1X). RagA$^{(\Delta/\Delta)Int}$ offspring had no detectable RagA after 2 weeks of tamoxifen treatment and no differences in body weight, villus length, or crypt architecture from RagA$^{(+/+)Int}$ littermates (Figure S1X). However, as in mTOR$^{(\Delta/\Delta)Int}$ and MCRS1$^{(\Delta/\Delta)Int}$ mice, mTORC1 activity was abolished, apoptosis was increased, and chromosomal aberrations were detected (aCGH, 27 ± 11 breaks) (Figure S1X).

Moreover, daily intraperitoneal injection of C57BL/6 mice for 2 weeks with deforolimus, a specific mTORC1 inhibitor, reduced mTORC1 activity (dephosphorylation of S6, 4EBP1, and CAD) and induced CIN in intestinal tissues (aCGH, 115 ± 86 breaks) (Figure S1Y). Deforolimus treatment also raised CIN levels in HCT-116 cells (Figure S1Z). Thus, mTORC1 inactivation induces DNA damage and chromosomal aberrations, impairing the proliferative capacity of the tissue in a CDK4/6-dependent manner but independently of WNT activation. Finally, fluorescein isothiocyanate (FITC)-dextran assays indicate that these perturbations increase intestinal barrier permeability in MCRS1$^{(\Delta/\Delta)Int}$ and mTOR$^{(\Delta/\Delta)Int}$ mice (Figure 1S).

MCRS1 and p53 Deletion Increases DNA Damage and CIN

To further probe links between mTORC1 inactivation-induced DNA damage, CIN, and intestinal homeostasis defects, MCRS1$^{(+/\Delta)Int}$ mice were crossed with p53$^{lox/lox}$ mice (here named MCRS1$^{(+/\Delta)Int}$; p53$^{(\Delta/\Delta)Int}$ mice) (Figure 2A) to increase DNA damage and CIN, reduce apoptosis, and release the proliferative break, as seen by reexpressing the dominant active kinases CDK4 and CDK6 (Figures 1K, 1L, and 1P). After 2 weeks of tamoxifen treatment, MCRS1$^{(+/\Delta)Int}$; p53$^{(\Delta/\Delta)Int}$ mice had less CAD activity, higher DNA damage and proliferation, but reduced apoptosis compared with MCRS1$^{(+/\Delta)Int}$; p53$^{(+/+)Int}$ mice. Consistent with increased DNA damage, these mice had also more chromosomal aberrations (aCGH, 28 ± 21 breaks) (Figures 2B–2G). The correlations between DNA damage, proliferation, and chromosomal aberrations suggest that aberrant cells acquire additional mutations while proliferating.

mTORC1/S6K1 inactivation-reduced CAD phosphorylation may putatively generate CIN due to insufficient deoxynucleotide synthesis (Ben-Sahra et al., 2013, 2016; Bester et al., 2011; Robitaille et al., 2013). Accordingly, tamoxifen-treated mouse embryonic fibroblasts (MEFs) from crosses of MCRS1$^{lox/lox}$ and Tg-UQ-CreERT2 mice (Fawal et al., 2015) had lower MCRS1 levels and mTORC1 inactivation and more chromosomal aberrations than non-treated MEFs (Figures S2A–S2C). However, supplementation of tamoxifen-treated MEFs with deoxynucleotides halved aCGH scores (from 84 to 48 breaks, Figure S3D). Thus, mTORC1 inactivation promotes CIN through deoxynucleotide deficiency, likely via reductions in CAD phosphorylation (Ben-Sahra et al., 2013, 2016; Bester et al., 2011; Robitaille et al., 2013).

mTORC1 Activity Is Important for Intestinal Tissue Homeostasis and Regeneration

Irradiating MCRS1$^{(+/+)Int}$ and mTOR$^{(+/+)Int}$ mice at 14 Gy caused increases in DNA damage and p53 levels, followed by rapid intestinal regeneration, hyper-proliferation, and regrowth of crypts within 72 hr (Figures 3A and S3A–S3E). However, recovery was severely impaired in irradiated MCRS1$^{(\Delta/\Delta)Int}$ and mTOR$^{(\Delta/\Delta)Int}$ mice, in which Ki67 staining and crypt counts revealed sharp reductions in intestinal regeneration capacity (Figures 3B–3D). Similarly, hyper-proliferation, rapid intestinal regeneration, and crypt regrowth were detected in irradiated RagA$^{(+/+)Int}$ mice, while responses were much weaker in RagA$^{(\Delta/\Delta)Int}$ mice 72 hr post irradiation (Figures S3F–S3H).

We also used a severe colitis model, induced by 30–50 kDa dextran sulfate sodium (DSS), a pro-inflammatory reagent that

(F) Representative aCGH from MCRS1$^{(+/\Delta)Int}$; p53$^{(\Delta/\Delta)Int}$ intestines 2 weeks after MCRS1 and p53 deletion (n = 3). Affected chromosomes are highlighted in bold red.

(G) Comparison of chromosomal breaks between MCRS1$^{(+/\Delta)Int}$; p53$^{(+/+)Int}$ and MCRS1$^{(+/\Delta)Int}$; p53$^{(\Delta/\Delta)Int}$ mice (n = 3).

Data are represented as means ± SEM; *p ≤ 0.05, ***p ≤ 0.001 (Student's t tests); scale bars 25 μm and 10 μm (B), at least 50 crypts (C, D, and E) were analyzed in each independent experiment. See also Figure S2.

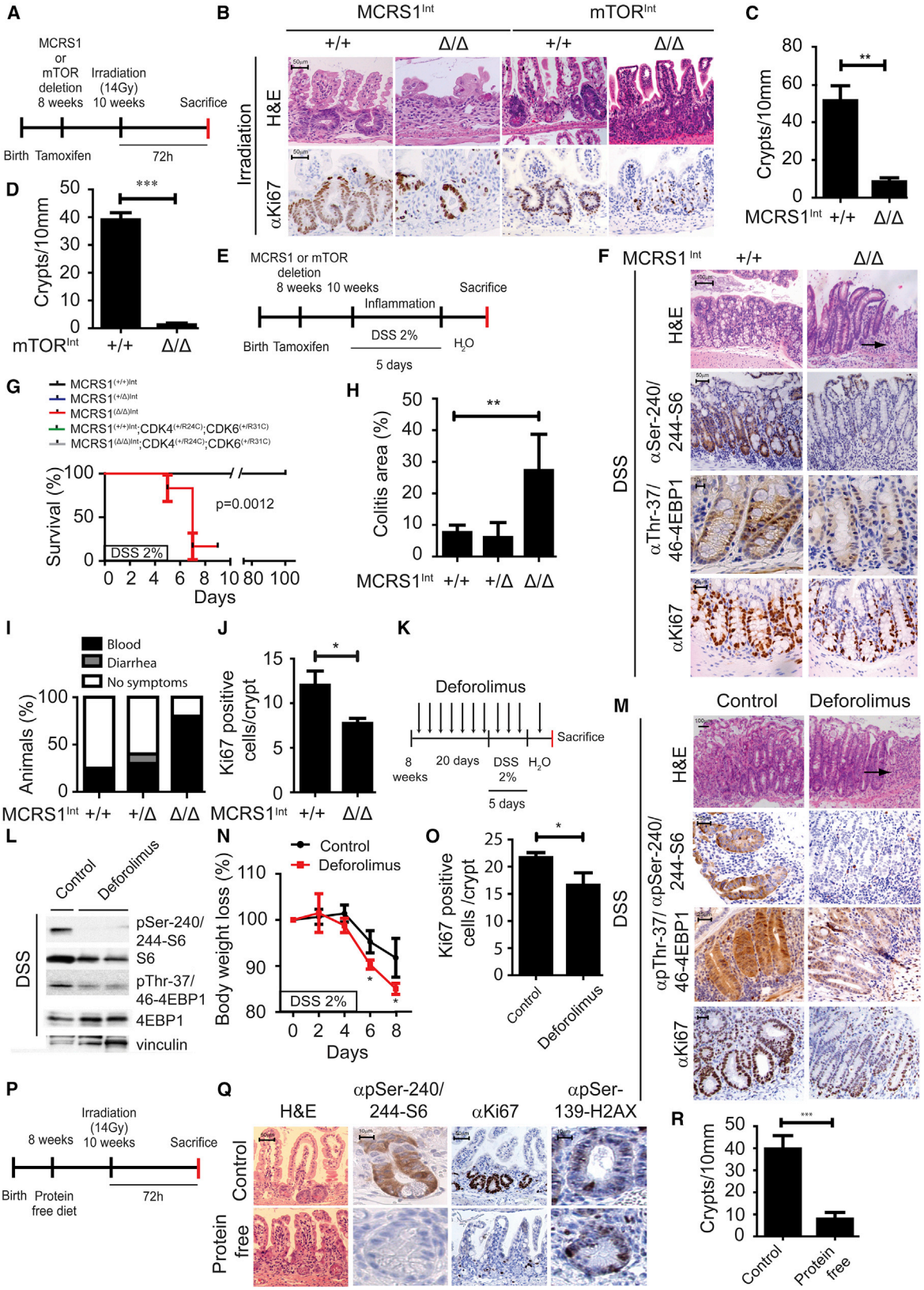

(legend on next page)

induces colonic mucosal permeability in mice (Perse and Cerar, 2012). mTOR$^{(+/+)Int}$ mice given 2% DSS in drinking water for 5 days recover through rapid tissue regeneration (Chassaing et al., 2014) (Figure 3E), but, after 5 days of DSS treatment, mTOR$^{(\Delta/\Delta)Int}$ mice suffered significant weight loss and impaired recovery, and died 3 weeks later following another round of DSS treatment (Figures S3I and S3J). MCRS1$^{(\Delta/\Delta)Int}$ mice with inactive mTORC1 also displayed significant weight loss, more severe colitis, and less proliferation in crypts than MCRS1$^{(+/+)Int}$ mice, and died after acute 2% DSS treatment (Figures 3E–3J and S3K). However, reinstating proliferative capacity by reactivating CDK4 and CDK6 kinases avoided their death (Figure 3G).

Inhibiting mTORC1 activity by intraperitoneally injecting DSS-treated C57BL/6 mice with deforolimus or torin 1 (an inhibitor of both mTOR complexes) every other day also resulted in significant body weight loss compared with controls (Figures 3K–3N, S3L, and S3M). Further, proliferation in crypts and regeneration of colonic epithelium were more rapid in control mice after DSS treatment than in mice treated with either inhibitor (Figures 3M, 3O, S3N, and S3O). Moreover, when C57BL/6 mice were given a chow or protein-free diet to inhibit mTORC1, then irradiated at 14 Gy, intestinal crypts re-grew in mice on chow, but intestinal regeneration was impaired in mice on the protein-free diet 72 hr later (Figures 3P–3R). Thus, a protein-free diet may impair intestinal regenerative capacity by inhibiting mTORC1.

We next tested effects of MCRS1 overexpression, using a *collagen α1(I)* knockin mouse (designated MCRS1$^{(+/KI)Int}$), expressing Flag-tagged human MCRS1 (hMCRS1) via a tetracycline-dependent transactivator controlled by the villin promoter (Roth et al., 2009) (Figures S3P–S3R). MCRS1$^{(+/+)Int}$ littermates lack hMCRS1 expression. When given doxycycline, MCRS1$^{(+/KI)Int}$ mice expressed hMCRS1 specifically in intestinal epithelium from 4 weeks onward (Figure S3S). MCRS1$^{(+/KI)Int}$ mice and littermates had normal body weight and intestinal architecture, but, in MCRS1$^{(+/KI)Int}$ mice, acute DSS treatment induced faster colon regeneration associated with increased mTORC1 activation (Figures S3T–S3X), confirming mTORC1's importance for intestinal tissue homeostasis and regeneration.

Long-Term mTORC1 Inactivation Triggers Reparative Inflammation

Next, we analyzed long-term consequences of mTORC1 inactivation associated with failure of intestinal homeostasis. In crypts of MCRS1$^{(\Delta/\Delta)Int}$ mice, 10 weeks after MCRS1 deletion, mTORC1 was inactive, proliferation was still reduced, and apoptosis increased (Figures S4A–S4D). There were no signs of inflammation 2 weeks after MCRS1 deletion. However, 10 weeks after tamoxifen treatment, MCRS1$^{(\Delta/\Delta)Int}$ mice had significantly more T cells (CD3ε positive), but not F4/80-positive macrophages, in intestinal tissue than MCRS1$^{(+/+)Int}$ mice (Figures S4B, S4E, and S4F), suggesting that low proliferation and high apoptosis precede inflammation.

Twenty weeks after MCRS1 deletion and mTORC1 inactivation, AKT phosphorylation at Ser-473 was slightly increased, but no differences in AMPK phosphorylation were detected and immune infiltrates (T cells and macrophages) were significantly higher in MCRS1$^{(\Delta/\Delta)Int}$ than in MCRS1$^{(+/+)Int}$ mouse intestines (Figures 4A–4D). Further, crypt hyper-proliferation was detected in MCRS1$^{(\Delta/\Delta)Int}$ mice, and apoptosis rates (measured by CC3 staining) were significantly lower than at 2 weeks, although qRT-PCR measurements of apoptosis modulators did not significantly differ between the time points (Figures 4B, 4E–4G, and S4G). Thus, inflammation precedes enhanced crypt cell proliferation and can lead to reduced apoptosis.

IL-6, a pro-inflammatory cytokine involved in intestinal disorders, was significantly upregulated in MCRS1$^{(\Delta/\Delta)Int}$ mice 20 weeks after MCRS1 deletion but not after 10 weeks, when we detected no increase in macrophage numbers (Figures 4H, S4B, S4F, and S4H). Thus, macrophages may be IL-6 sources in these mice, as in a colitis-associated carcinogenesis mouse model (Grivennikov et al., 2009). Moreover, downstream IL-6 targets implicated in tissue regeneration, such as STAT3 phosphorylated at Tyr-705 and YAP (Taniguchi et al., 2015), were elevated in MCRS1$^{(\Delta/\Delta)Int}$ mouse intestines 20 weeks after MCRS1 deletion (Figures 4B and 4I–4K). Further, expression of HES1, a Notch target gene targeted by YAP, increased in the intestinal epithelium of MCRS1$^{(\Delta/\Delta)Int}$ mice (Figures 4B, 4K, and 4L), suggesting ongoing tissue regeneration. Moreover, the intestinal barrier was not disrupted when mTORC1 was inactivated at this time (Figure S4I). Thus, long-term mTORC1 inactivation leads to wound healing and tissue regeneration, possibly in a non-cell-autonomous manner involving inflammation-associated IL-6/STAT3/YAP signaling.

Chromosomal breaks were more frequent at 20 weeks than 2 weeks post MCRS1 deletion (aCGH: 30 ± 13 and 11 ± 8 breaks, respectively) (Figures S4J and S4K), suggesting accumulation of chromosomal aberrations. However, we detected no significant differences in WNT activation at any stage (Figure S4L), so long-term mTORC1 inactivation apparently leads to tissue regeneration and increases in chromosomal aberrations independently of canonical WNT activation.

To further test inflammation's capacity to induce intestinal regeneration, we chronically treated MCRS1$^{(+/+)Int}$, MCRS1$^{(+/\Delta)Int}$, and MCRS1$^{(\Delta/\Delta)Int}$ mice with lower DSS doses, allowing some MCRS1$^{(\Delta/\Delta)Int}$ mice to survive (three 1-week cycles of 1.5% DSS, once per month) (Figure S4M). Consistent

Figure 3. mTORC1 Activity Is Important for Intestinal Tissue Homeostasis and Regeneration

(A–D) Scheme of irradiation (A), H&E and IHC (B), and quantification of crypts in MCRS1^{Int} (n = 4) (C) and mTOR^{Int} (n = 4) (D) intestines.

(E–J) Scheme of DSS treatment (E), H&E and IHC of colon sections (F), Kaplan-Meier curve (G), quantification of colitis area based on H&E of colon sections (H), percentage of mice with diarrhea or rectal bleeding (I), and quantification of Ki67 IHC (J) from (F) in MCRS1^{Int} mice (n = 6).

(K–O) Schematic representation (K), western blot of colons (L), H&E and IHC in colon sections (M), percentage of body weight loss (N), and quantification of Ki67 (O) from (M) from C57BL/6 mice treated with acute DSS combined with deforolimus (n = 4).

(P–R) Scheme of irradiation (P), H&E and IHC (Q), and quantification of crypts in intestinal sections (R) from mice treated with protein-free diet (n = 6).

Data are represented as means ± SEM; *$p \leq 0.05$, **$p \leq 0.01$, ***$p \leq 0.001$ (Student's t tests). Scale bars, 50 μm (B); 100 μm, 50 μm, 25 μm, and 10 μm (F); or 100 μm and 25 μm (M). Arrowhead indicates colitis area (F and M); at least 50 crypts (C, D, J, O, and R) were analyzed in each independent experiment. See also Figure S3.

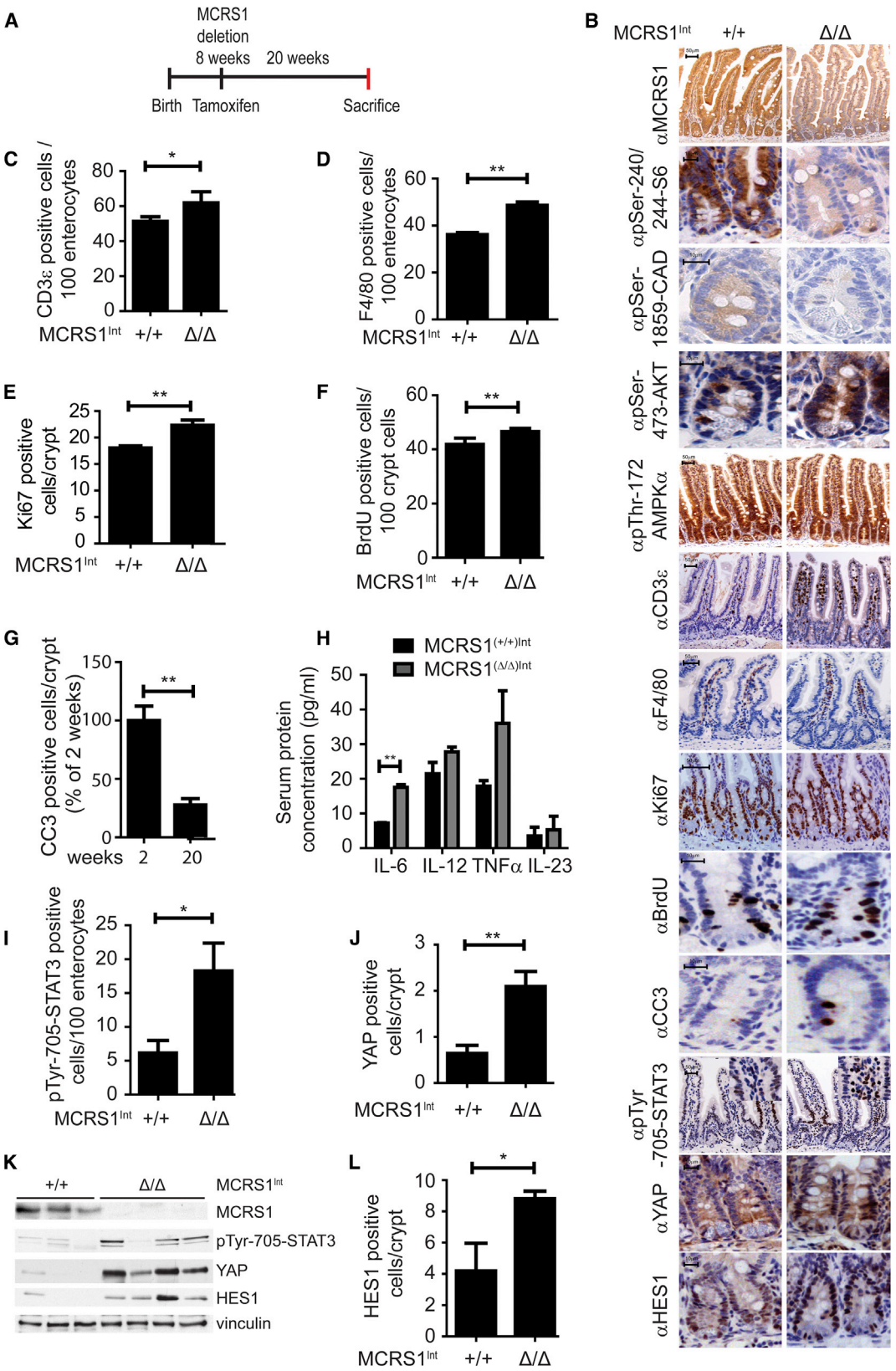

(legend on next page)

with increased intestinal hyper-proliferative capacity, MCRS1$^{(\Delta/\Delta)Int}$ mice had normal colonic epithelia after the last DSS treatment round, with increased DNA damage and activation of the IL-6-associated signaling pathways implicated in regeneration (Figures S4N–S4Q). CIN was also increased in colonic tissues of DSS-treated MCRS1$^{(\Delta/\Delta)Int}$ mice (FISH score, 1.4 ± 0.46, Figures S4R and S4S).

Long-Term mTORC1 Inactivation Triggers Spontaneous Intestinal Adenomas and Enhances Chemically Induced CRC

Concordant with increases in chromosomal breaks in MCRS1$^{(\Delta/\Delta)Int}$ mice, intestinal crypt fission (which initiates polyp formation) was detected 20 weeks after the deletion (Figures S4J and S4K). Ten percent of the mice developed spontaneous intestinal polyps that remained MCRS1 negative, had reduced mTORC1 (but not AMPK) activity, and had slightly increased AKT phosphorylation at Ser-473 (Figures 5A and 5B). Tumorigenesis incidence is similar (<10%) in IBD patients (Kanneganti et al., 2011), suggesting that MCRS1$^{(\Delta/\Delta)Int}$ mice with inactivated mTORC1 recapitulate some colitis-induced CRC steps. We detected no spontaneous tumors in DSS-treated MCRS1$^{(\Delta/\Delta)Int}$ mouse colons, possibly due to the short treatment time (120 days in total), low DSS dose (1.5%), differences between intestines and colons, and low incidence of spontaneous tumors.

We thus accelerated CRC associated with chronic inflammation using the azoxymethane (AOM)/DSS model, which mimics human colitis-associated CRC resulting in multiple large adenomas around 10–12 weeks after initial AOM injection (Neufert et al., 2007). Acute 2% DSS treatment killed MCRS1$^{(\Delta/\Delta)Int}$ mice within a week via intestinal regeneration failure (Figure 3G), so MCRS1$^{(+/+)Int}$ and MCRS1$^{(+/\Delta)Int}$ mice were intraperitoneally injected with 7.5 mg/kg of AOM, given three 1-week cycles (one per month) of 2% DSS in drinking water, then killed 100 days after AOM injection (Figure 5C) (Neufert et al., 2007). MCRS1$^{(+/\Delta)Int}$ mice had higher tumor burdens, in frequency, size, and grade, than MCRS1$^{(+/+)Int}$ mice after AOM/DSS treatment (Figures 5D–5G) and their polyps had less MCRS1 and mTORC1 activation, with stronger proliferation, apoptosis, and inflammation. Levels of serum IL-6 and associated downstream effectors were also elevated in tumors from AOM/DSS-treated MCRS1$^{(+/\Delta)Int}$ mice (Figures S5A–S5C). Tumor grades of mice killed at 200 days excluded presence of carcinomas (Figure S5D), suggesting that MCRS1 deletion in combination with AOM/DSS is insufficient to promote transition to aggressive carcinoma. Further, colons of mice with deletion of MCRS1 after AOM/DSS treatment, in which MCRS1 expression and mTORC1 activation were abolished, had more polyps and bigger and more aggressive tumors than MCRS1$^{(+/+)Int}$ mice (Figures S5E and S5F). Thus, MCRS1-deletion-induced mTORC1 inactivation promotes tumorigenesis.

AOM/DSS-treated MCRS1$^{(+/\Delta)Int}$ mice also had more chromosomal aberrations (FISH, CIN score, 1.8 ± 0.52; aCGH, 107 ± 71 breaks) than non-treated MCRS1$^{(\Delta/\Delta)Int}$ mice (aCGH, 30 ± 13 breaks) with lower tumor incidence (10%) after 20 weeks of tamoxifen treatment (Figures 5B and 5H–5K). Thus, MCRS1-deletion-induced mTORC1 inactivation increases tumorigenesis, correlating with increases in chromosomal breaks.

mTOR$^{(+/\Delta)Int}$ mice treated with AOM/DSS also resulted in bigger, more aggressive tumors (including grade 4 carcinomas) with lower mTOR activity than mTOR$^{(+/+)Int}$ littermates but had similar numbers of polyps per colon (Figures 5L–5O and S5G). Moreover, their tumors had significantly more chromosomal aberrations (FISH, CIN score 1.53 ± 0.31; aCGH, 30 ± 15 breaks) (Figures 5P–5R). Notably, proliferation was not affected but apoptosis was increased in these tumors (Figure S5H), suggesting that cells with high CIN levels can undergo apoptosis. Hence, mTOR deletion induces CRC, correlating with increased DNA damage and CIN.

AOM/DSS treatment of RagA$^{(\Delta/\Delta)Int}$ mice, which survived DSS treatment alone (not shown), also resulted in more aggressive tumors, with more chromosomal aberrations (aCGH, 34 ± 6 breaks) but of similar size to those in treated RagA$^{(+/+)Int}$ mice (Figures S5I–S5K). These data suggest that mTORC1 inactivation induces CRC, correlating with increased DNA damage and CIN and corroborating findings with MCRS1^{Int} and mTOR^{Int} mice. Accordingly, crosses of MCRS1$^{(+/\Delta)Int}$ and p53$^{lox/lox}$ mice with high DNA damage and CIN levels (Figures 2C, 2F, and 2G) had significantly higher tumor burdens than MCRS1$^{(+/\Delta)Int}$ mice (Figures 5S and 5T). Thus, proliferating cells with inactivated mTORC1 accumulate DNA damage and chromosomal aberrations, possibly leading to tumorigenesis.

In tests of whether mTORC1 activation protects against inflammation-induced CRC, MCRS1-overexpressing MCRS1$^{(+/KI)Int}$ mice subjected to AOM/DSS treatment had significantly fewer tumors, with stronger mTORC1 activation and ameliorated IL-6 signaling, than AOM/DSS-treated controls (Figures S5L–S5N). Further, to check if dietary activation of mTORC1 protects against AOM/DSS-induced carcinogenesis, C57BL/6 mice were injected with AOM and supplied drinking water containing 2% DSS with (DSS^{WP}) or without whey protein (Figure S5O), a dietary supplement with high levels of mTORC1-stimulating amino acids (Bar-Peled and Sabatini, 2014). Colons from AOM/DSS^{WP}-treated mice exhibited mTORC1 hyperactivity (increased S6 and 4EBP1 phosphorylation) and developed similar numbers of polyps, but of significantly smaller and lower

Figure 4. Long-Term mTORC1 Inactivation Triggers Reparative Inflammation

(A) Scheme of tamoxifen-treated MCRS1^{Int} mice.

(B–G) IHC (B) and quantifications of CD3ε (C), F4/80 (D), Ki67 (E), bromodeoxyuridine (BrdU) (F), and CC3 (G) in MCRS1$^{(+/+)Int}$ (n = 11) and MCRS1$^{(\Delta/\Delta)Int}$ (n = 10) intestines 20 weeks after MCRS1 deletion.

(H) Serum IL-6, IL-12, tumor necrosis factor alpha (TNF-α), and IL-23 levels from MCRS1$^{(+/+)Int}$ (n = 11) and MCRS1$^{(\Delta/\Delta)Int}$ (n = 10) mice killed 20 weeks after MCRS1 deletion.

(I and J) Quantification of pTyr-705-STAT3 (I) and YAP (J) IHC from (B).

(K) WB of MCRS1^{Int} intestines 20 weeks after MCRS1 deletion.

(L) Quantification of HES1 IHC from (B).

Data are represented as means ± SEM; *p ≤ 0.05, **p ≤ 0.01 (Student's t tests); scale bars, 50 μm or 10 μm (B); at least 50 crypts (E, F, G, J, and L) or villi (C, D, and I) were analyzed in each independent experiment. See also Figure S4 and Table S1.

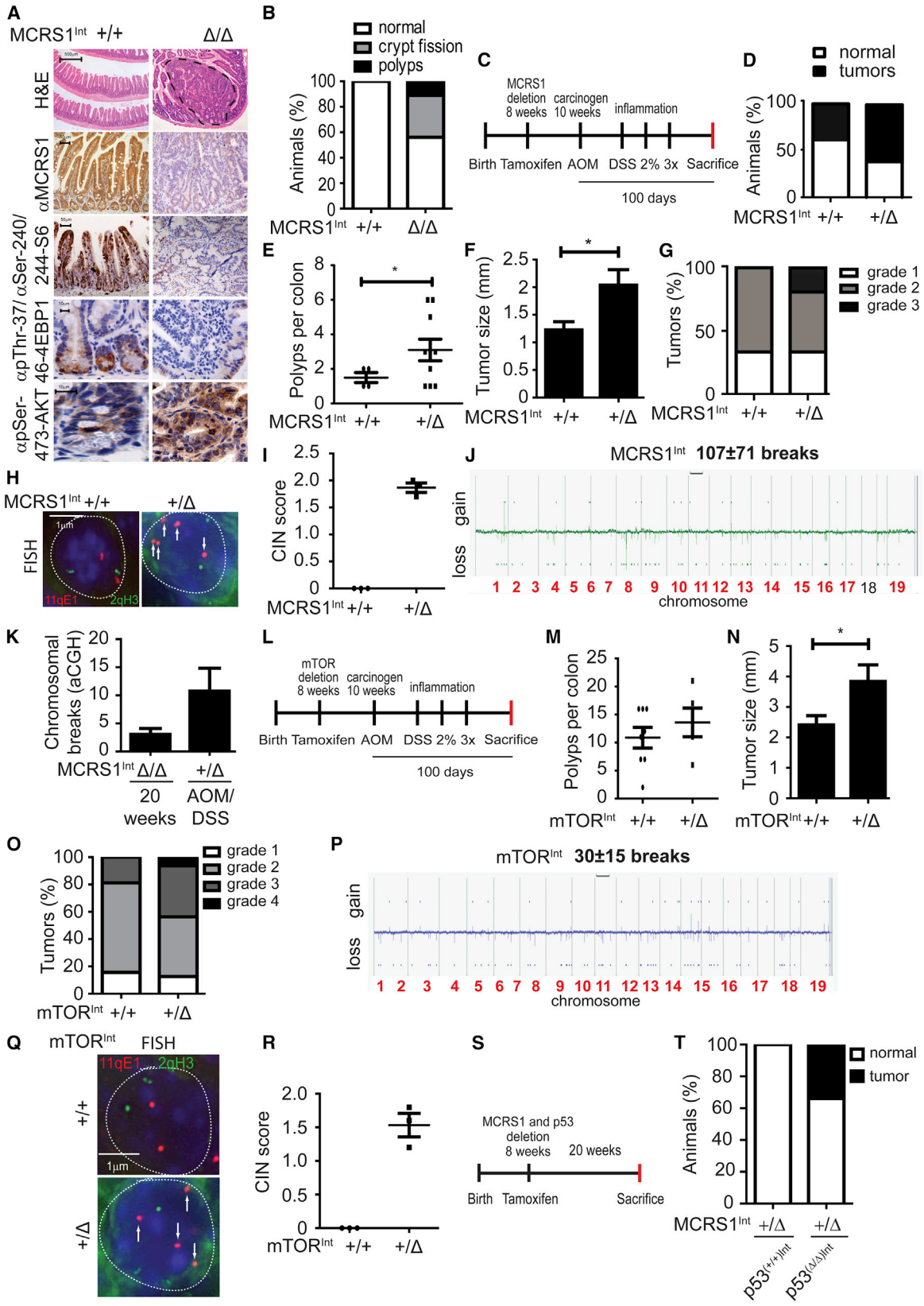

(legend on next page)

grade, than AOM/DSS-treated controls (Figures S5O–S5T), suggesting that mTORC1 activation has tumor-suppressive effects in colitis-associated CRC. Mice treated with acute, deleterious concentrations of DSS or DSS^{WP} (3%) for 5 days showed increased mTORC1 activation and similar body weight loss (Figure S5U), so DSS is active in combination with whey protein. Thus, mTORC1 activation is essential for preventing colitis-induced CRC.

Analysis of WNT signaling in mTORC1-inactivated tumors with high CIN and inflammation showed that WNT/β-catenin target gene expression was significantly weaker in AOM/DSS-induced tumors than in tumors arising from *Apc* mutations in the genetic CRC model (Figure 7 and STAR Methods; Figure S5V). Further, deep sequencing revealed no *Apc* gene variants in them (Figures S5W and S5X). Thus, tumors arising from high inflammation due to mTORC1 inactivation are likely generated by DNA damage and accumulation of chromosomal aberrations rather than WNT/β-catenin activation. Canonical WNT activation may occur in late stages, as indicated by patchy nuclear β-catenin staining in spontaneous tumors from MCRS1$^{(\Delta/\Delta)Int}$ mice and tumors from AOM/DSS-treated MCRS1$^{(+/\Delta)Int}$ and mTOR$^{(+/\Delta)Int}$ mice (Figures S5Y and S5Z), suggesting partial β-catenin translocation. This also suggests that, in colitis-induced CRC, canonical WNT activation is not a driver but a late event. Thus, mTORC1 inactivation generates DNA damage and high CIN, which may cause CRC synergistically with inflammation-associated IL-6, independently of WNT signaling.

Blocking Inflammation and IL-6 Signaling Abolishes mTORC1-Inactivation-Induced CRC

Supplying sulindac (a broad anti-inflammatory reagent) in drinking water to MCRS1$^{(\Delta/\Delta)Int}$ mice with inactivated mTORC1 significantly reduced (relative to controls receiving reagent-free water) inflammation, serum IL-6 levels, downstream IL-6 effectors, and crypt compartment hyper-proliferation to levels in sulindac-treated MCRS1$^{(+/+)Int}$ mice (Figures 6A–6F and S6A–S6C). Apoptosis levels were similar in sulindac-treated MCRS1$^{(\Delta/\Delta)Int}$ mice and mice treated with reagent-free water (Figure 6G).

Further, blocking IL-6 signaling in MCRS1$^{(\Delta/\Delta)Int}$ mice, using an anti-IL-6 receptor (IL-6R) (clone MR16-1) for 20 weeks (Okazaki et al., 2002) reduced crypt cell proliferation, compared with levels in untreated MCRS1$^{(\Delta/\Delta)Int}$ mice (Figures 6H, 6I, S6D, and S6E). No aberrant intestinal structures, such as crypt fission, or tumors were detected in MCRS1$^{(\Delta/\Delta)Int}$ mice treated with the antibody (not shown). Thus, we subjected MCRS1$^{(+/+)Int}$ and MCRS1$^{(+/\Delta)Int}$ mice to the AOM/DSS treatment described above, in combination with sulindac treatment or injections for 100 days with the anti-IL-6R (MR16-1) antibody or a specific IL-6-neutralizing antibody (Figure 6J). Sulindac and IL-6 signaling blockers reduced tumorigenesis in MCRS1$^{(+/\Delta)Int}$ mice to levels in control mice (Figures 6K and S6F). Thus, reducing inflammation and IL-6 levels can reduce crypt hyper-proliferation, restore intestinal homeostasis, and prevent chronic inflammation and CRC in mice with inactivated mTORC1.

mTORC1 Inactivation Reduces Tumor Incidence in APC Mice

We then crossed MCRS1$^{lox/lox}$ mice and conditional *Apc*-mutant, *Apc*(15lox)/FabplCre, mice (Robanus-Maandag et al., 2010) to check whether mTORC1 inhibition may affect tumorigenesis in a non-inflammatory genetic CRC model, driven by canonical WNT pathway activation. Cre-mediated deletion, directed to the intestinal epithelium, was initiated as early as embryonic day 13.5 using the FabplCre mouse (Robanus-Maandag et al., 2010) (Figure 7A). Double mutants had improved survival (Figure 7B), and at 100 days, heterozygous deletion of *Apc* induced multiple tumors via WNT activation, mainly in the colon and distal small intestine (Figure 7C). However, double-mutant MCRS1$^{lox/lox}$/*Apc*(15lox)/FabplCre mice had lower tumor burdens: 50% were tumor free at 100 days, while almost all *Apc*(15lox)/FabplCre mice had tumors, significantly fewer polyps per intestine, and lower grades of similar-sized tumors (Figures 7C–7E and S7A). Further, tumors from double-mutant mice were MCRS1 negative, exhibited mTORC1 inactivation, and all their tumoral tissue stained positive for nuclear β-catenin (Figure S7B). Forty percent of double-mutant mice killed at 5 months were still tumor free, had lower tumor grades, had less mTORC1

Figure 5. Long-Term mTORC1 Inactivation Triggers Spontaneous Intestinal Adenomas and Enhances Chemically Induced CRC

(A) H&E and IHC from MCRS1$^{(+/+)Int}$ (n = 11) and MCRS1$^{(\Delta/\Delta)Int}$ (n = 10) intestines 20 weeks after MCRS1 deletion.
(B) Percentage of intestinal abnormalities in H&E of MCRS1$^{(+/+)Int}$ (n = 11) and MCRS1$^{(\Delta/\Delta)Int}$ (n = 10) intestines 20 weeks after MCRS1 deletion.
(C) Scheme of AOM/DSS-treated MCRS1^{Int} mice.
(D–G) Percentage of mice with colorectal polyps (D); number of polyps (E); tumor size (F); and percentage of colorectal tumors of grade 1, 2, or 3 (G) based on H&E of colon sections from MCRS1$^{(+/+)Int}$ (n = 10) and MCRS1$^{(+/\Delta)Int}$ (n = 17) mice treated with AOM/DSS.
(H) FISH with 11qE1 (red) and 2qH3 (green) probes in colon sections from MCRS1$^{(+/+)Int}$ (n = 3) and MCRS1$^{(+/\Delta)Int}$ (n = 3) mice treated with AOM/DSS.
(I) Quantification of CIN from (H).
(J) Representative aCGH from colons of MCRS1^{Int} mice treated with AOM/DSS (n = 3). Affected chromosomes are highlighted in bold red.
(K) Comparison of chromosomal breaks detected in MCRS1$^{(\Delta/\Delta)Int}$ (n = 3) mice 20 weeks after MCRS1 deletion and AOM/DSS-treated MCRS1$^{(+/\Delta)Int}$ (n = 3) mice.
(L) Scheme of AOM/DSS-treated mTOR^{Int} mice killed 100 days after carcinogen injection.
(M–O) Number of polyps (M); tumor size (N); and percentage of colorectal tumors of grade 1, 2, 3, or 4 (O) based on H&E of AOM/DSS-treated mTOR$^{(+/+)Int}$ (n = 8) and mTOR1$^{(+/\Delta)Int}$ (n = 5) colons.
(P) Representative aCGH from colons of mTOR^{Int} mice treated with AOM/DSS (n = 3). Affected chromosomes are highlighted in bold red.
(Q) FISH with 11qE1 (red) and 2qH3 (green) probes in AOM/DSS-treated mTOR$^{(+/+)Int}$ (n = 3) and mTOR$^{(+/\Delta)Int}$ (n = 3) colons.
(R) Quantification of CIN from (Q).
(S and T) Scheme (S) and percentage of mice with intestinal polyps (T) in MCRS1^{Int} and MCRS1^{Int}; p53$^{(\Delta/\Delta)Int}$ mice killed 20 weeks after MCRS1 and p53 deletion (n = 3).
Data are represented as means ± SEM; *p ≤ 0.05 (Student's t tests). Scale bars, 500 μm, 50 μm, or 10 μm (A); 1 μm (H and Q). At least 100 nuclei (H, I, Q, and R) were analyzed in each independent experiment; arrowheads indicate CIN (H and Q); white dashed line highlights single nucleus (H and Q). See also Figure S5 and Table S1.

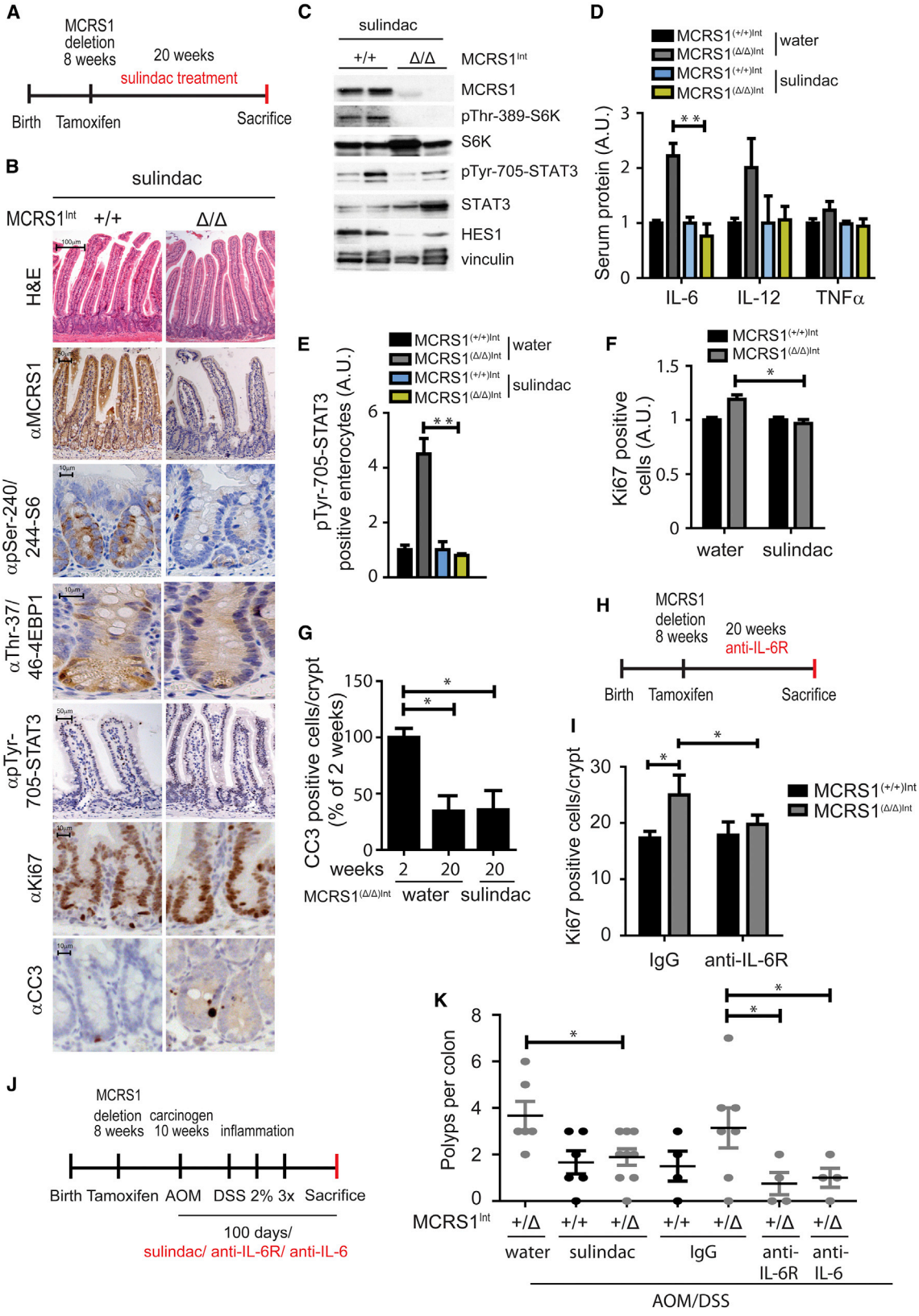

(legend on next page)

activation than controls, and stained positive for nuclear β-catenin (Figures 7C–7E, S7A, S7C, and S7D), with no signs of inflammation or increases in pro-inflammatory cytokines (Figure S7E). Moreover, *Apc*(15lox)/FabplCre mice treated with deforolimus for 100 days had smaller tumors than non-treated mice but similar numbers of polyps (Figures S7F–S7J).

Interestingly, CIN levels in double mutants were high at 100 days (FISH score, 2.03 ± 1; aCGH, 35 ± 22 breaks) but much lower at 5 months (FISH score, 0.5 ± 0.87) and negatively correlated with tumor incidence (Figures 7F–7H). We also deleted MCRS1 and APC in adult mice, by crossing $MCRS1^{lox/lox}$ and *Apc*(15lox)/Villin-CreERT2 mice. The resulting $MCRS1^{(\Delta/\Delta)Int}$; $APC^{(+/\Delta)Int}$ mice had more chromosomal aberrations than $MCRS1^{(\Delta/\Delta)Int}$; $APC^{(+/+)Int}$ mice (aCGH, 3 ± 1.5 breaks) after 2 weeks of tamoxifen treatment (Figures S7K and S7L). Thus, conversely to colitis-induced CRC, mTORC1 inactivation has tumor-preventive activities and protects against WNT/β-catenin activation-dependent CRC, possibly due to the higher levels of chromosomal aberrations that occur when MCRS1 and APC deletion is combined.

We also crossed $MCRS1^{lox/lox}$ and FabplCre mice and found (as in MCRS1-deleted adult Villin-CreERT2 mice; Figures 5C–5G) that AOM/DSS treatment of mice with embryonic deletion of MCRS1 increased tumor incidence, size, and grade (Figures S7M–S7Q). Moreover, mTORC1 was inactivated, and DNA damage and CIN were increased in tumors of these mice (Figures S7R and S7S). Hence, inflammation-driven tumorigenesis in MCRS1 mouse models is not dependent on specific Cre lines or time of MCRS1 deletion, and mTORC1's role (oncogenic or tumor suppressive) depends on the presence of colitis and *Apc* mutations.

MCRS1 Is Lost in Human IBD and Inversely Correlates with Inflammation in Human CRC

Analysis of human colon tissues from 23 IBD patients (14 with UC, 9 with CD), 8 healthy controls, and 6 adjacent non-affected controls showed that MCRS1 expression was reduced in colons from IBD patients (Figures 7I–7K). Further, tissue microarrays from 208 CRC patients and 16 non-tumoral tissues revealed negative correlations between MCRS1 expression and both overall inflammation (CD45 staining) and macrophage levels (CD68 and CD163 staining) (Figures 7L–7N and S7T). We also detected inverse correlations between mTORC1 activation and inflammation markers (CD45, CD68, and CD163) (Figures 7O, S7U, and S7V). MCRS1 expression is positively associated with mTORC1 activation and poor prognosis in these samples (Fawal et al., 2015). Thus, increased MCRS1 and mTORC1 activation correlate with low inflammation in CRC. Further analyses of these CRC samples revealed a positive correlation between MCRS1 expression and nuclear β-catenin staining (Figures 7P and S7W). Thus, mTORC1 may have oncogenic or tumor-suppressive activities depending on the CRC tumor type and association with canonical WNT activation (Figure S7X).

DISCUSSION

MCRS1 links nutrient surpluses to mTORC1 activation (Fawal et al., 2015). Its ablation in intestinal epithelium inhibits mTORC1 activation, promoting DNA damage and chromosomal aberrations, decreasing crypt proliferation capacity by inhibiting the CDK4/CKD6 axis, and increasing apoptosis, thus impairing tissue regeneration. Accordingly, DNA damage activates p53 and abolishes CDK4/CDK6/pRB/E2F axis activity (Ewen et al., 1995; He et al., 2005), suggesting it precedes proliferation defects. Cyclins E/A, E2F target genes, are also downregulated in $MCRS1^{(\Delta/\Delta)Int}$ mice, enabling cell-cycle arrest. Cyclin E/CDK2 complexes phosphorylate $p27^{Kip1}$, targeting it for degradation by E3 ubiquitin ligase SKP2, thus promoting cyclin A expression, allowing S phase and cell-cycle progression (Sutterluty et al., 1999). Cyclin E/CDK2 and CDK4/6 complex kinases also phosphorylate and inhibit retinoblastoma protein (pRB), promoting activation of the E2F transcriptional factor driving cells to S phase through G1 phase, and constitutively expressed cyclins A/E can overcome pRb-mediated suppression of proliferation (Hinds et al., 1992). MCRS1 depletion reduces CDK4/6 levels, pRB phosphorylation, E2F activity, and thus cyclin A/E levels, all affecting cell-cycle progression. Further, abolishing p53 or expressing dominant active CDK4/CDK6 kinases in MCRS1-depleted mice restores crypt proliferation capacity and increases CIN and tumorigenesis. Our data suggest that anti-inflammatory agents could improve the efficacy of CDK4/6 inhibitors, such as palbociclib, as emerging therapeutics for CRC (Ziemke et al., 2016).

DNA damage and CIN are associated with aneuploidy and may provide selective advantage in the inflammatory milieu, enabling cancer cells to escape homeostasis mechanisms and contribute to tumorigenesis. Aneuploidies have long been recognized as chromosomal aberrations in tumorigenesis (Williams and Amon, 2009), but our data suggest that CIN and aneuploidy may be drivers of inflammation-requiring tumorigenesis. Thus, cancer cells may increase chromosomal instabilities by coopting the DNA damage response, as illustrated in mice with inactivated mTORC1 and deleted p53, which show high DNA damage and CIN, with drastically increased CRC incidence. Moreover, loss

Figure 6. Blocking Inflammation and IL-6 Signaling Abolishes mTORC1 Inactivation-Induced CRC

(A) Scheme of sulindac treatment in $MCRS1^{Int}$ mice.

(B) H&E and IHC from sulindac-treated $MCRS1^{Int}$ intestines (n = 4).

(C) WB of sulindac-treated $MCRS1^{Int}$ intestines (n = 4).

(D) Serum IL-6, IL-12, and TNF-α levels in sulindac-treated $MCRS1^{Int}$ mice (n = 4).

(E–G) Quantification of pTyr-705-STAT3 (E), Ki67 (F), and CC3 (G) IHC from (B) (n = 4).

(H and I) Scheme (H) and quantification of Ki67 IHC (I) from $MCRS1^{(+/+)Int}$ (n = 4) and $MCRS1^{(\Delta/\Delta)Int}$ (n = 4) mice treated with immunoglobulin G (IgG) or anti-IL6 receptor (IL-6R) antibody.

(J and K) Scheme (J) and number of polyps based on H&E of colon sections (K) from $MCRS1^{Int}$ mice treated with AOM/DSS and water (n = 6), sulindac ($MCRS1^{(+/+)Int}$ [n = 6] and $MCRS1^{(+/\Delta)Int}$ [n = 9]), IgG ($MCRS1^{(+/+)Int}$ [n = 4] and $MCRS1^{(+/\Delta)Int}$ [n = 7]), anti-IL-6R (n = 4), and anti-IL-6 (n = 4).

Data are represented as means ± SEM; $^*p \leq 0.05$, $^{**}p \leq 0.01$ (Student's t tests); scale bars, 100 μm, 50 μm, or 10 μm (B); at least 50 crypts (F, G, and I) or villi (E) were analyzed in each independent experiment. See also Figure S6.

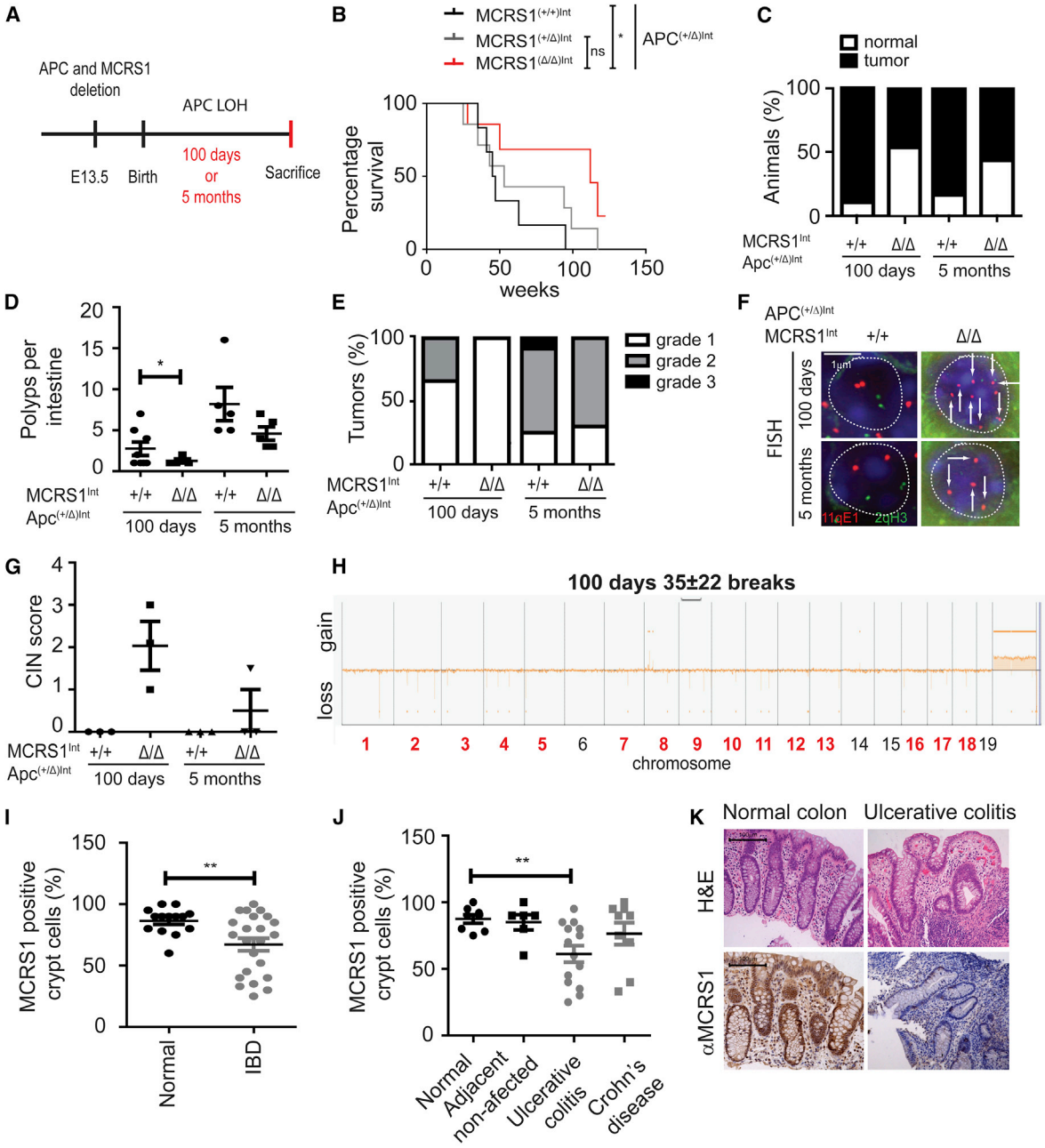

(legend on next page)

or reduction in mice of BUB1 (a serine/threonine kinase that establishes the mitotic spindle during the mitosis checkpoint and chromosomal segregation) promotes CIN-induced aneuploidy and tumorigenesis in mice heterozygous for $p53^{+/-}$ or $Apc^{Min/+}$ (Baker et al., 2009; Jeganathan et al., 2007; Schliekelman et al., 2009). Haploinsufficiency of BubR1, another mitotic checkpoint protein, also raises the incidence of colon tumors in $Apc^{Min/+}$ mice (Rao et al., 2005). Thus, CIN-induced aneuploidy levels are key tumorigenesis factors. Too much CIN may lead to mitotic catastrophe or burdens of detrimental mutations that activate surveillance mechanisms and target cells for death; e.g., polypoid cancer cells in mice can trigger immune responses that limit tumor growth (Senovilla et al., 2012). Low or moderate CIN levels may allow proliferation of aberrant cells, leading (with inflammation) to tumorigenesis, as in the colitis model. CIN scores of our $mTOR^{Int}$ and $MCRS1^{Int}$ model mice suggest they have few chromosomal aberrations but enough to provide genetic variations and promote CRC in cooperation with IL-6, independently of canonical WNT activation. In such contexts, *Apc* mutations are not drivers but may occur in the last stage of tumor development. mTORC1 inactivation in mutated *Apc* background abolishes CRC, thus, together with mTORC1 inhibition, *Apc* mutations may lead to excessive DNA damage and CIN, followed by targeting of aberrant cells for apoptosis and suppression of tumor growth. There is evidence in humans for a "serrated-polyp pathway" (largely independent of the classic adenoma-to-carcinoma sequence) to CRC, but genetic instability is likely a rate-limiting step causing quick neoplastic evolution (Jass, 2005). Further, increases in DNA damage are putatively critical for induction of chromosomal aberrations in human serrated adenomas (Jass, 2005). These reports are consistent with our findings, although mTORC1 status remains to be determined in these tumors.

Long-term mTORC1 inactivation triggers (apparently WNT independently) chronic reparative inflammation through IL-6 production, restoring crypt proliferation and promoting tissue regeneration, wound healing, and spontaneous CRC induced by chromosomal aberrations. Acute inflammation is a crucial, evolutionarily conserved, protective response in the routine regeneration of injured tissues, but aberrant and chronic reparative inflammation may cause severe pathologies, including CRC (Karin and Clevers, 2016). Immune cells respond to cell death, especially necrotic death, and tissue damage causing release of damage-associated molecular patterns that initiate and perpetuate non-infectious inflammatory responses (Karin and Clevers, 2016; Lamkanfi and Dixit, 2012). For example, the inflammatory switch from cancer inhibition to cancer promotion reportedly results from persistent DNA damage that triggers senescence, followed by the inflammatory response and intestinal neoplasia (Pribluda et al., 2013). However, we detected no senescence in our model.

When intestinal barrier integrity is affected, inflammatory signaling cascades that promote wound healing, regeneration, and CRC development can also be triggered by pathogen-associated molecular patterns released by intestinal bacteria (Escamilla-Tilch et al., 2013; Karin and Clevers, 2016). Thus, nutrient imbalances may influence intestinal epithelium homeostasis (rather than the dysbiosis per se), generating a milieu where microbiota may activate immune responses and cause IBD-induced CRC. MCRS1 mice may be useful for studying interactive roles of mTORC1 regulation, nutrient imbalances, and microbiota in IBD-induced CRC, but we need more knowledge of associations between intestinal barrier disruption, microbiome activation, and inflammatory cell recruitment to intestinal epithelia.

Various cytokines can induce IBD immunopathogenesis and CRC (Karin and Clevers, 2016), particularly IL-6, which triggers crypt hyper-proliferation that restores tissue regeneration and promotes colorectal tumors (Grivennikov et al., 2009). Sources of IL-6 in our model are not known, but lamina propria, macrophages, and dendritic cells are major sources during intestinal mucosa injury (Karin and Clevers, 2016). Thus, targeting IL-6 signaling is valuable, but broader nonsteroidal anti-inflammatory drugs may have strong carcinogenesis-suppressing effects, and further investigation of IL-6-dependent inflammatory cascades may reveal new therapeutic strategies for IBD-associated CRC.

Maintaining healthy nutrition is difficult for IBD patients due to disease symptoms, complications, appetite-changing medications and impairments in food intake, assimilation, digestion, and nutrient absorption. Long-term nutrient imbalances or deficiencies may inactivate the mTORC1 pathway, increasing their risks of developing CRC. Our results suggest that high-protein diets could reduce tumor burdens in patients with chronic

Figure 7. mTORC1 Inactivation Reduces Tumor Incidence in APC Mice

(A) Scheme of APC mice crossed with $MCRS1^{Int}$ mice.

(B) Kaplan-Meier curve of $Apc^{(+/\Delta)Int}$; $MCRS1^{(+/+)Int}$ (n = 6), $Apc^{(+/\Delta)Int}$; $MCRS1^{(+/\Delta)Int}$ (n = 7), and $Apc^{(+/\Delta)Int}$; $MCRS1^{(\Delta/\Delta)Int}$ (n = 7) mice.

(C–E) Percentage of mice with intestinal tumors (C), number of polyps (D), and percentage of intestinal tumors of grade 1, 2, or 3 (E) from $Apc^{(+/\Delta)Int}$; $MCRS1^{(+/+)Int}$ (n = 10) and $Apc^{(+/\Delta)Int}$; $MCRS1^{(\Delta/\Delta)Int}$ (n = 11) mice killed at 100 days and $Apc^{(+/\Delta)Int}$; $MCRS1^{(+/+)Int}$ (n = 10) and $Apc^{(+/\Delta)Int}$; $MCRS1^{(\Delta/\Delta)Int}$ (n = 10) mice killed at 5 months.

(F) FISH with 11qE1 (red) and 2qH3 (green) probes in intestinal sections from $Apc^{(+/\Delta)Int}$; $MCRS1^{(+/+)Int}$ (n = 10) and $Apc^{(+/\Delta)Int}$; $MCRS1^{(\Delta/\Delta)Int}$ (n = 11) mice killed at 100 days and $Apc^{(+/\Delta)Int}$; $MCRS1^{(+/+)Int}$ (n = 10) and $Apc^{(+/\Delta)Int}$; $MCRS1^{(\Delta/\Delta)Int}$ (n = 10) mice killed at 5 months.

(G) Quantification of CIN from (F).

(H) Representative aCGH from intestines from $Apc^{(+/\Delta)Int}$; $MCRS1^{(\Delta/\Delta)Int}$ (n = 3) mice killed at 100 days. Affected chromosomes are highlighted in bold red.

(I and J) Quantification of MCRS1 IHC in control (n = 14) and human IBD patients (n = 23) (I), and control (n = 8), adjacent non-affected (n = 6), UC (n = 14), and CD (n = 9) tissue from patients (J).

(K) H&E and IHC of samples from control (n = 8) and human UC patients (n = 14).

(L–P) Stratification of human colorectal tumors (n = 208) according to CD45 and MCRS1 (L) CD68 and MCRS1 (M), CD163 and MCRS1 (N), pSer-240/244-S6 and CD45 (O), and MCRS1 and β-catenin (P) staining.

Data are represented as means ± SEM; $^{*}p \leq 0.05$, $^{**}p \leq 0.01$ (Student's t tests); scale bars, 1 μm (F) or 100 μm (K); at least 50 crypts (I and J) and at least 100 nuclei (F and G) were analyzed in each independent experiment; arrowheads indicate CIN (F), white dashed line highlights single nucleus (F). See also Figure S7 and Table S1.

gastrointestinal inflammation. Further, IBD medications (e.g., corticosteroids) that mainly reduce inflammation are generally more effective in people with good nutrition, so supplementation with a rich-protein source (e.g., whey protein) may protect IBD patients from secondary effects of anti-inflammatory drug therapies and prevent CRC development, especially during steroid treatments.

The mTOR inhibitor AZD8055 reduces DSS-induced colitis in mice through anti-inflammatory effects mediated via T helper cell polarization and proliferation (Hu et al., 2016). Further, RAD001 (a rapamycin derivative) reduces AOM/DSS-induced CRC by restricting inflammation in mice (Thiem et al., 2013). Thus, administration of mTORC1 inhibitors has immunosuppressive inflammation- and tumorigenesis-reducing effects. In further concordance with our results, mTORC1 inhibition by rapamycin impairs intestinal cell proliferation, induces cell apoptosis, and inhibits intestinal regeneration (Guan et al., 2015). Clearly, mTORC1 activation in intestinal epithelium may suppress tumorigenesis in IBD patients who develop CRC via chromosomal aberrations rather than canonical WNT activation, but it may promote oncogenesis in patients with *APC* mutations (Faller et al., 2015). Hence, supplementation with a rich-protein source (e.g., whey protein) may prevent CRC in IBD patients, while a low-protein diet may offer CRC prophylactic options for patients with genetic predispositions such as *APC* mutations. Our findings have important implications for the clinical use of mTORC1 inhibitors in patients with acute IBD and open new avenues to optimized and personalized therapeutic regimens for CRC.

STAR★METHODS

Detailed methods are provided in the online version of this paper and include the following:

- KEY RESOURCES TABLE
- CONTACT FOR REAGENT AND RESOURCE SHARING
- EXPERIMENTAL MODEL AND SUBJECT DETAILS
  - Mouse Models
  - Intestine Preparation
  - Tumor Quantification
  - Human Samples
  - Cell Culture
- METHOD DETAILS
  - Mouse Diets and Treatments
  - Fluorescence *In Situ* Hybridization
  - CIN Analysis
  - aCGH Analysis
  - Immunohistochemistry and Histology
  - Senescence-Associated β-Galactosidase Assay
  - Immunoblotting
  - Serum Cytokine Measurement
  - ROS, ATP and mtDNA Measurement
  - *Apc* Gene Sequencing
  - Genotyping and qRT-PCR
- QUANTIFICATION AND STATISTICAL ANALYSIS
  - Image Analysis
  - Statistical Analysis
- DATA AND SOFTWARE AVAILABILITY

SUPPLEMENTAL INFORMATION

Supplemental Information includes seven figures and three tables and can be found with this article online at https://doi.org/10.1016/j.cmet.2017.11.006.

AUTHOR CONTRIBUTIONS

M.B. designed, performed, and analyzed most of the experiments and data. M.B. and N.D. engineered the MCRS1^{lox} allele (Fawal et al., 2015). T.P.G. performed experiments and analyzed data. K.S.T., M.-A.F., and N.D. engineered the Col1a1hMCRS1 allele. R.T.-R. and S.R.-P. performed and analyzed FISH and aCGH. C.P. analyzed the histology of mouse and human tissues. N.D. analyzed data; designed the experiments; and conceived, developed, and wrote the project and the manuscript. Funding was secured by N.D.

ACKNOWLEDGMENTS

We thank R. Smits for providing the Villin-rtTA, APC15lox, and FabplCre mice; S. Kozma for giving us the mTOR$^{lox/lox}$ mouse; A. Efeyan for giving us the RagA$^{lox/lox}$ mouse; E. Wagner for giving us the p53$^{lox/lox}$ mouse; and M. Malumbres for providing us with CDK4-R24C/CDK6-R31C mice. We are also very thankful to Dr. Tadamitsu Kishimoto and Dr. Yoshihiro Matsumoto as well as Chugai Pharmaceutical Co., Ltd. for supplying the anti-IL6R (MR16-1) antibody. We thank A. Efeyan, M. Malumbres, and M. Perez-Moreno for critical reading of this manuscript. M.B. is a recipient of La Caixa PhD fellowship. N.D. is a recipient of the Spanish Ramón y Cajal fellowship. This work was supported by the Spanish Ministry of Economy and Competitiveness and co-funded by ERDF-EU (FEDER, SAF2016-76598-R) and by the Olga Torres Foundation (FOT).

Received: June 7, 2017
Revised: August 21, 2017
Accepted: November 15, 2017
Published: December 21, 2017

REFERENCES

Baker, D.J., Jin, F., Jeganathan, K.B., and van Deursen, J.M. (2009). Whole chromosome instability caused by Bub1 insufficiency drives tumorigenesis through tumor suppressor gene loss of heterozygosity. Cancer Cell *16*, 475–486.

Bar-Peled, L., and Sabatini, D.M. (2014). Regulation of mTORC1 by amino acids. Trends Cell Biol. *24*, 400–406.

Beard, C., Hochedlinger, K., Plath, K., Wutz, A., and Jaenisch, R. (2006). Efficient method to generate single-copy transgenic mice by site-specific integration in embryonic stem cells. Genesis *44*, 23–28.

Ben-Sahra, I., Howell, J.J., Asara, J.M., and Manning, B.D. (2013). Stimulation of de novo pyrimidine synthesis by growth signaling through mTOR and S6K1. Science *339*, 1323–1328.

Ben-Sahra, I., Hoxhaj, G., Ricoult, S.J., Asara, J.M., and Manning, B.D. (2016). mTORC1 induces purine synthesis through control of the mitochondrial tetrahydrofolate cycle. Science *351*, 728–733.

Bester, A.C., Roniger, M., Oren, Y.S., Im, M.M., Sarni, D., Chaoat, M., Bensimon, A., Zamir, G., Shewach, D.S., and Kerem, B. (2011). Nucleotide deficiency promotes genomic instability in early stages of cancer development. Cell *145*, 435–446.

Boivin, G.P., Washington, K., Yang, K., Ward, J.M., Pretlow, T.P., Russell, R., Besselsen, D.G., Godfrey, V.L., Doetschman, T., Dove, W.F., et al. (2003). Pathology of mouse models of intestinal cancer: consensus report and recommendations. Gastroenterology *124*, 762–777.

Brenner, H., Kloor, M., and Pox, C.P. (2014). Colorectal cancer. Lancet *383*, 1490–1502.

Burrell, R.A., McClelland, S.E., Endesfelder, D., Groth, P., Weller, M.C., Shaikh, N., Domingo, E., Kanu, N., Dewhurst, S.M., Gronroos, E., et al. (2013). Replication stress links structural and numerical cancer chromosomal instability. Nature *494*, 492–496.

Chassaing, B., Aitken, J.D., Malleshappa, M., and Vijay-Kumar, M. (2014). Dextran sulfate sodium (DSS)-induced colitis in mice. Curr. Protoc. Immunol. *104*. Unit 15.25.

Clevers, H. (2013). The intestinal crypt, a prototype stem cell compartment. Cell *154*, 274–284.

Cunningham, J.T., Rodgers, J.T., Arlow, D.H., Vazquez, F., Mootha, V.K., and Puigserver, P. (2007). mTOR controls mitochondrial oxidative function through a YY1-PGC-1alpha transcriptional complex. Nature *450*, 736–740.

Djouder, N., Metzler, S.C., Schmidt, A., Wirbelauer, C., Gstaiger, M., Aebersold, R., Hess, D., and Krek, W. (2007). S6K1-mediated disassembly of mitochondrial URI/PP1gamma complexes activates a negative feedback program that counters S6K1 survival signaling. Mol. Cell *28*, 28–40.

Dowling, R.J., Topisirovic, I., Alain, T., Bidinosti, M., Fonseca, B.D., Petroulakis, E., Wang, X., Larsson, O., Selvaraj, A., Liu, Y., et al. (2010). mTORC1-mediated cell proliferation, but not cell growth, controlled by the 4E-BPs. Science *328*, 1172–1176.

Efeyan, A., Schweitzer, L.D., Bilate, A.M., Chang, S., Kirak, O., Lamming, D.W., and Sabatini, D.M. (2014). RagA, but not RagB, is essential for embryonic development and adult mice. Dev. Cell *29*, 321–329.

el Marjou, F., Janssen, K.P., Chang, B.H., Li, M., Hindie, V., Chan, L., Louvard, D., Chambon, P., Metzger, D., and Robine, S. (2004). Tissue-specific and inducible Cre-mediated recombination in the gut epithelium. Genesis *39*, 186–193.

Escamilla-Tilch, M., Filio-Rodriguez, G., Garcia-Rocha, R., Mancilla-Herrera, I., Mitchison, N.A., Ruiz-Pacheco, J.A., Sanchez-Garcia, F.J., Sandoval-Borrego, D., and Vazquez-Sanchez, E.A. (2013). The interplay between pathogen-associated and danger-associated molecular patterns: an inflammatory code in cancer? Immunol. Cell Biol. *91*, 601–610.

Ewen, M.E., Oliver, C.J., Sluss, H.K., Miller, S.J., and Peeper, D.S. (1995). p53-dependent repression of CDK4 translation in TGF-beta-induced G1 cell-cycle arrest. Genes Dev. *9*, 204–217.

Faller, W.J., Jackson, T.J., Knight, J.R., Ridgway, R.A., Jamieson, T., Karim, S.A., Jones, C., Radulescu, S., Huels, D.J., Myant, K.B., et al. (2015). mTORC1-mediated translational elongation limits intestinal tumour initiation and growth. Nature *517*, 497–500.

Fawal, M.A., Brandt, M., and Djouder, N. (2015). MCRS1 binds and couples rheb to amino acid-dependent mTORC1 activation. Dev. Cell *33*, 67–81.

Francipane, M.G., and Lagasse, E. (2014). mTOR pathway in colorectal cancer: an update. Oncotarget *5*, 49–66.

Grivennikov, S., Karin, E., Terzic, J., Mucida, D., Yu, G.Y., Vallabhapurapu, S., Scheller, J., Rose-John, S., Cheroutre, H., Eckmann, L., and Karin, M. (2009). IL-6 and Stat3 are required for survival of intestinal epithelial cells and development of colitis-associated cancer. Cancer Cell *15*, 103–113.

Guan, Y., Zhang, L., Li, X., Zhang, X., Liu, S., Gao, N., Li, L., Gao, G., Wei, G., Chen, Z., et al. (2015). Repression of mammalian target of rapamycin complex 1 inhibits intestinal regeneration in acute inflammatory bowel disease models. J. Immunol. *195*, 339–346.

Gulhati, P., Cai, Q., Li, J., Liu, J., Rychahou, P.G., Qiu, S., Lee, E.Y., Silva, S.R., Bowen, K.A., Gao, T., and Evers, B.M. (2009). Targeted inhibition of mammalian target of rapamycin signaling inhibits tumorigenesis of colorectal cancer. Clin. Cancer Res. *15*, 7207–7216.

He, G., Siddik, Z.H., Huang, Z., Wang, R., Koomen, J., Kobayashi, R., Khokhar, A.R., and Kuang, J. (2005). Induction of p21 by p53 following DNA damage inhibits both Cdk4 and Cdk2 activities. Oncogene *24*, 2929–2943.

Hinds, P.W., Mittnacht, S., Dulic, V., Arnold, A., Reed, S.I., and Weinberg, R.A. (1992). Regulation of retinoblastoma protein functions by ectopic expression of human cyclins. Cell *70*, 993–1006.

Hoshii, T., Kasada, A., Hatakeyama, T., Ohtani, M., Tadokoro, Y., Naka, K., Ikenoue, T., Ikawa, T., Kawamoto, H., Fehling, H.J., et al. (2014). Loss of mTOR complex 1 induces developmental blockage in early T-lymphopoiesis and eradicates T-cell acute lymphoblastic leukemia cells. Proc. Natl. Acad. Sci. USA *111*, 3805–3810.

Hsu, C.C., Lee, Y.C., Yeh, S.H., Chen, C.H., Wu, C.C., Wang, T.Y., Chen, Y.N., Hung, L.Y., Liu, Y.W., Chen, H.K., et al. (2012). 58-kDa microspherule protein (MSP58) is novel Brahma-related gene 1 (BRG1)-associated protein that modulates p53/p21 senescence pathway. J. Biol. Chem. *287*, 22533–22548.

Hu, S., Chen, M., Wang, Y., Wang, Z., Pei, Y., Fan, R., Liu, X., Wang, L., Zhou, J., Zheng, S., et al. (2016). mTOR inhibition attenuates dextran sulfate sodium-induced colitis by suppressing T cell proliferation and balancing TH1/TH17/Treg profile. PLoS One *11*, e0154564.

Jass, J.R. (2005). Serrated adenoma of the colorectum and the DNA-methylator phenotype. Nat. Clin. Pract. Oncol. *2*, 398–405.

Jeganathan, K., Malureanu, L., Baker, D.J., Abraham, S.C., and van Deursen, J.M. (2007). Bub1 mediates cell death in response to chromosome missegregation and acts to suppress spontaneous tumorigenesis. J. Cell Biol. *179*, 255–267.

Kanneganti, M., Mino-Kenudson, M., and Mizoguchi, E. (2011). Animal models of colitis-associated carcinogenesis. J. Biomed. Biotechnol. *2011*, 342637.

Karin, M., and Clevers, H. (2016). Reparative inflammation takes charge of tissue regeneration. Nature *529*, 307–315.

Lamkanfi, M., and Dixit, V.M. (2012). Inflammasomes and their roles in health and disease. Annu. Rev. Cell Dev. Biol. *28*, 137–161.

Liko, D., and Hall, M.N. (2015). mTOR in health and in sickness. J. Mol. Med. *93*, 1061–1073.

Montagne, J., Stewart, M.J., Stocker, H., Hafen, E., Kozma, S.C., and Thomas, G. (1999). *Drosophila* S6 kinase: a regulator of cell size. Science *285*, 2126–2129.

Neufert, C., Becker, C., and Neurath, M.F. (2007). An inducible mouse model of colon carcinogenesis for the analysis of sporadic and inflammation-driven tumor progression. Nat. Protoc. *2*, 1998–2004.

Okazaki, M., Yamada, Y., Nishimoto, N., Yoshizaki, K., and Mihara, M. (2002). Characterization of anti-mouse interleukin-6 receptor antibody. Immunol. Lett. *84*, 231–240.

Perse, M., and Cerar, A. (2012). Dextran sodium sulphate colitis mouse model: traps and tricks. J. Biomed. Biotechnol. *2012*, 718617.

Pribluda, A., Elyada, E., Wiener, Z., Hamza, H., Goldstein, R.E., Biton, M., Burstain, I., Morgenstern, Y., Brachya, G., Billauer, H., et al. (2013). A senescence-inflammatory switch from cancer-inhibitory to cancer-promoting mechanism. Cancer Cell *24*, 242–256.

Rao, C.V., Yang, Y.M., Swamy, M.V., Liu, T., Fang, Y., Mahmood, R., Jhanwar-Uniyal, M., and Dai, W. (2005). Colonic tumorigenesis in BubR1+/-ApcMin/+ compound mutant mice is linked to premature separation of sister chromatids and enhanced genomic instability. Proc. Natl. Acad. Sci. USA *102*, 4365–4370.

Risson, V., Mazelin, L., Roceri, M., Sanchez, H., Moncollin, V., Corneloup, C., Richard-Bulteau, H., Vignaud, A., Baas, D., Defour, A., et al. (2009). Muscle inactivation of mTOR causes metabolic and dystrophin defects leading to severe myopathy. J. Cell Biol. *187*, 859–874.

Robanus-Maandag, E.C., Koelink, P.J., Breukel, C., Salvatori, D.C., Jagmohan-Changur, S.C., Bosch, C.A., Verspaget, H.W., Devilee, P., Fodde, R., and Smits, R. (2010). A new conditional Apc-mutant mouse model for colorectal cancer. Carcinogenesis *31*, 946–952.

Robitaille, A.M., Christen, S., Shimobayashi, M., Cornu, M., Fava, L.L., Moes, S., Prescianotto-Baschong, C., Sauer, U., Jenoe, P., and Hall, M.N. (2013). Quantitative phosphoproteomics reveal mTORC1 activates de novo pyrimidine synthesis. Science *339*, 1320–1323.

Rodriguez-Diez, E., Quereda, V., Bellutti, F., Prchal-Murphy, M., Partida, D., Eguren, M., Kollmann, K., Gomez de Cedron, M., Dubus, P., Canamero, M., et al. (2014). Cdk4 and Cdk6 cooperate in counteracting the INK4 family of inhibitors during murine leukemogenesis. Blood *124*, 2380–2390.

Rodriguez-Perales, S., Torres-Ruiz, R., Suela, J., Acquadro, F., Martin, M.C., Yebra, E., Ramirez, J.C., Alvarez, S., and Cigudosa, J.C. (2016). Truncated RUNX1 protein generated by a novel t(1;21)(p32;q22) chromosomal translocation impairs the proliferation and differentiation of human hematopoietic progenitors. Oncogene *35*, 125–134.

Roth, S., Franken, P., van Veelen, W., Blonden, L., Raghoebir, L., Beverloo, B., van Drunen, E., Kuipers, E.J., Rottier, R., Fodde, R., and Smits, R. (2009). Generation of a tightly regulated doxycycline-inducible model for studying mouse intestinal biology. Genesis *47*, 7–13.

Saam, J.R., and Gordon, J.I. (1999). Inducible gene knockouts in the small intestinal and colonic epithelium. J. Biol. Chem. *274*, 38071–38082.

Sampson, L.L., Davis, A.K., Grogg, M.W., and Zheng, Y. (2016). mTOR disruption causes intestinal epithelial cell defects and intestinal atrophy postinjury in mice. FASEB J. *30*, 1263–1275.

Schliekelman, M., Cowley, D.O., O'Quinn, R., Oliver, T.G., Lu, L., Salmon, E.D., and Van Dyke, T. (2009). Impaired Bub1 function in vivo compromises tension-dependent checkpoint function leading to aneuploidy and tumorigenesis. Cancer Res. *69*, 45–54.

Senovilla, L., Vitale, I., Martins, I., Tailler, M., Pailleret, C., Michaud, M., Galluzzi, L., Adjemian, S., Kepp, O., Niso-Santano, M., et al. (2012). An immunosurveillance mechanism controls cancer cell ploidy. Science *337*, 1678–1684.

Sutterluty, H., Chatelain, E., Marti, A., Wirbelauer, C., Senften, M., Muller, U., and Krek, W. (1999). p45SKP2 promotes p27Kip1 degradation and induces S phase in quiescent cells. Nat. Cell Biol. *1*, 207–214.

Taniguchi, K., Wu, L.W., Grivennikov, S.I., de Jong, P.R., Lian, I., Yu, F.X., Wang, K., Ho, S.B., Boland, B.S., Chang, J.T., et al. (2015). A gp130-Src-YAP module links inflammation to epithelial regeneration. Nature *519*, 57–62.

Thiem, S., Pierce, T.P., Palmieri, M., Putoczki, T.L., Buchert, M., Preaudet, A., Farid, R.O., Love, C., Catimel, B., Lei, Z., et al. (2013). mTORC1 inhibition restricts inflammation-associated gastrointestinal tumorigenesis in mice. J. Clin. Invest. *123*, 767–781.

Thomas, J.D., Zhang, Y.J., Wei, Y.H., Cho, J.H., Morris, L.E., Wang, H.Y., and Zheng, X.F. (2014). Rab1A is an mTORC1 activator and a colorectal oncogene. Cancer Cell *26*, 754–769.

Tummala, K.S., Gomes, A.L., Yilmaz, M., Grana, O., Bakiri, L., Ruppen, I., Ximenez-Embun, P., Sheshappanavar, V., Rodriguez-Justo, M., Pisano, D.G., et al. (2014). Inhibition of de novo NAD(+) synthesis by oncogenic URI causes liver tumorigenesis through DNA damage. Cancer Cell *26*, 826–839.

Wang, X.W., and Zhang, Y.J. (2014). Targeting mTOR network in colorectal cancer therapy. World J. Gastroenterol. *20*, 4178–4188.

Williams, B.R., and Amon, A. (2009). Aneuploidy: cancer's fatal flaw? Cancer Res. *69*, 5289–5291.

Yang, J., Zhao, X., Patel, A., Potru, R., Azizi-Ghannad, S., Dolinger, M., Cao, J., Bartholomew, C., Mazurkiewicz, J., Conti, D., et al. (2015). Rapamycin inhibition of mTOR reduces levels of the Na+/H+ exchanger 3 in intestines of mice and humans, leading to diarrhea. Gastroenterology *149*, 151–162.

Yilmaz, O.H., Katajisto, P., Lamming, D.W., Gultekin, Y., Bauer-Rowe, K.E., Sengupta, S., Birsoy, K., Dursun, A., Yilmaz, V.O., Selig, M., et al. (2012). mTORC1 in the Paneth cell niche couples intestinal stem-cell function to calorie intake. Nature *486*, 490–495.

Zhang, Y.J., Dai, Q., Sun, D.F., Xiong, H., Tian, X.Q., Gao, F.H., Xu, M.H., Chen, G.Q., Han, Z.G., and Fang, J.Y. (2009). mTOR signaling pathway is a target for the treatment of colorectal cancer. Ann. Surg. Oncol. *16*, 2617–2628.

Ziemke, E.K., Dosch, J.S., Maust, J.D., Shettigar, A., Sen, A., Welling, T.H., Hardiman, K.M., and Sebolt-Leopold, J.S. (2016). Sensitivity of KRAS-mutant colorectal cancers to combination therapy that cotargets MEK and CDK4/6. Clin. Cancer Res. *22*, 405–414.

STAR★METHODS

KEY RESOURCES TABLE

REAGENT or RESOURCE	SOURCE	IDENTIFIER
Antibodies		
Goat polyclonal anti-CD3ε (M-20)	Santa Cruz Biotechnology	Cat#sc-1127; RRID: AB_631128
Goat polyclonal anti-phospho-RB (Ser-807/811)	Santa Cruz Biotechnology	Cat#sc-16670; RRID: AB_655250
Mouse monoclonal anti-5-Bromo-2-deoxyuridine (BrdU)	GE Healthcare	Cat# RPN202; RRID: AB_2314032
Mouse monoclonal anti-CD163	LEICA	Cat#NCL-L-CD163; RRID: AB_563
Mouse monoclonal anti-CDK6 (19G)	CNIO Monoclonal Antibodies Unit	Cat#AM-19G
Mouse monoclonal anti-cyclinD1 (A-12)	Santa Cruz Biotechnology	Cat#sc-8396; RRID: AB_627344
Mouse monoclonal anti-human CD45 ALC FLEX (2B11+PD7/26)	DAKO	Cat#IR751; RRID: AB_2661839
Mouse monoclonal anti-human CD68 FLEX (KP1)	DAKO	Cat#IR609; RRID: AB_2661840
Rabbit polyclonal anti-MCRS1	Dr. Nabil Djouder (Fawal et al., 2015)	N/A
Mouse monoclonal anti-PCNA (PC10)	Santa Cruz Biotechnology	Cat#sc-56; RRID: AB_628110
Mouse monoclonal anti-phospho-Histone H2A.X (Ser139) (JBW301)	Millipore	Cat#05-636; RRID: AB_309864
Mouse monoclonal anti-vinculin (hVIN-1)	Sigma-Aldrich	Cat#V9131; RRID: AB_477629
Mouse monoclonal anti-β-catenin	BD Biosciences	Cat#610153; RRID: AB_397554
Rabbit monoclonal anti-HES1 (D6P2U)	Cell Signaling Technology	Cat#11988
Rabbit monoclonal anti-Ki67 (SP6)	Master Diagnostica	Cat#MAD-000310QD
Rabbit monoclonal anti-mTOR (7C10)	Cell Signaling Technology	Cat#2983; RRID:AB_2105622
Rabbit monoclonal anti-phospho-4EBP1 (Thr-37/46) (236B4)	Cell Signaling Technology	Cat#2855; RRID: AB_560835
Rabbit monoclonal anti-phospho-AMPKα (Thr-172) (40H9)	Cell Signaling Technology	Cat#2535; RRID: AB_331250
Rabbit monoclonal anti-phospho-p70 S6 kinase1 (S6K1) (Thr-389) (108D2)	Cell Signaling Technology	Cat#9234; RRID: AB_2269803
Rabbit monoclonal anti-phospho-Stat3 (Tyr-705) (D3A7) XP	Cell Signaling Technology	Cat#9145; RRID: AB_2491009
Rabbit monoclonal anti-S6 Ribosomal Protein (5G10)	Cell Signaling Technology	Cat#2217; RRID: AB_331355
Rabbit monoclonal anti-YAP (D8H1X) XP	Cell Signaling Technology	Cat#14074; RRID: AB_331588
Rabbit polyclonal anti-4EBP1	Cell Signaling Technology	Cat#9452; RRID: AB_823410
Rabbit polyclonal anti-CDK4 (C-22)	Santa Cruz Biotechnology	Cat#sc-260; RRID: AB_631219
Rabbit polyclonal anti-Cleave Caspase-3 (CC3) (Asp-175)	Cell Signaling Technology	Cat#9661; RRID: AB_2341188
Rabbit polyclonal anti-p53 protein (CM5)	Vector Laboratories	Cat#VP-P956; RRID: AB_2335917
Rabbit polyclonal anti-phospho-AKT (Ser-473)	Cell Signaling Technology	Cat#9271; RRID: AB_329825
Rabbit polyclonal anti-phospho-CAD (Ser-1859)	Cell Signaling Technology	Cat#12662
Rabbit polyclonal anti-phospho-Histone H3 (Ser10)	Millipore	Cat#06-570; RRID: AB_310177
Rabbit polyclonal anti-phospho-p70-S6 Kinase1 (Thr-389)	Santa Cruz Biotechnology	Cat#sc-11759; RRID:AB_2238689
Rabbit polyclonal anti-phospho-S6- Ribosomal Protein (S6) (Ser-240/244)	Cell Signaling Technology	Cat#2215; RRID:AB_331682
Rabbit polyclonal anti-Stat3	Cell Signaling Technology	Cat#9132; RRID: AB_331588
Rat monoclonal anti-F4/80 (CI :A3-1)	CNIO Monoclonal Antibodies Unit	Cat#MCA497
Rat monoclonal anti-mouse IL-6 (MP5-20F3)	BioXCell	Cat#BE0046; RRID: AB_1107709
Rat monoclonal anti-mouse IL-6R (MR 16-1)	Tadamitsu Kishimoto and Chugai Pharmaceutical (Okazaki et al., 2002)	N/A
Rat Monoclonal IgG1 (anti-HRPN)	BioXCell	Cat#BE0088; RRID: AB_1107775

(*Continued on next page*)

Continued

REAGENT or RESOURCE	SOURCE	IDENTIFIER
Biological Samples		
Human: Crohn's disease (CD) samples	University Guadalajara Hospital	N/A
Human: colorectal cancer (CRC) samples	CNIO Biobank	N/A
Human: ulcerative colitis (UC) samples	University Guadalajara Hospital	N/A
Chemicals, Peptides, and Recombinant Proteins		
0.5% Glutaraldehyde	Sigma-Aldrich	G5882; CAS:111-30-8
100% Hydrolyzed hydropure whey protein extract	Amix	N/A
2-[N-morpholino]ethanesulphonic acid (MES)	Sigma-Aldrich	163732; CAS: 145224-94-8
2-mercaptoethanol	Sigma-Aldrich	M6250; CAS: 60-24-2
2-Propanol 99.7%	Panreac Quimica, S.L.U.	11610901214
30%(w/v) Acrylamide: 0.8% /9w/v) Bis-Acrylamide Stock Solution (37.5:1)	ProtoGel	EC-890
5-bromo-4-chloro-3-indolyl-â-D-galactopyranoside	Apollo Scientific	OR8235
Agarose Electrophoresis Grade	Apollo Scientific	BIA1176
Azoxymethane (AOM)	Sigma-Aldrich	A5486; CAS: 25843-45-2
Bovine Serum Albumin	Sigma-Aldrich	A7906; CAS: 9048-46-8
Bradford Protein Assay	BioRad	5000001
BrdU (5-Bromo-2'-deoxyuridine)	Sigma-Aldrich	19-160
Deforolimus	MedChem Express	AP23573**;** HY-50908
Dextran sulfate sodium salt (DSS), Molecular Weight 36,000-50,000	MP Biomedicals	02160110; CAS: 9011-18-1
Dimethyl sulfoxide (DMSO)	Sigma-Aldrich	276855; CAS: 67-68-5
Dimethylformamide	Sigma-Aldrich	A8625; CAS:7512-17-6
DMEM	Life Technologies, S.A.	31885-049
dNTP mix	Bioron	110001
Doxycycline Hyclate diet (200 mg/Kg)	Envigo	TD.04104
Ethylenediaminetetraacetic acid (EDTA)	Sigma-Aldrich	ED; CAS: 60-00-4
Fetal Bovine Serum	Sigma-Aldrich	F7524
Fluorescein isothiocyanate-dextran (FITC-dextran)	Sigma-Aldrich	46945; CAS: 60842-46-8
Formalin solution 10%	Panreac Quimica S.L.U	HT501128
Hydrogen Peroxide Solution	Sigma-Aldrich	H1009; CAS: 7722-84-1
Hydroxytamoxifen	Sigma-Aldrich	H6278; CAS: 68392-35-8
Isocaloric protein free diet	Envigo	TD.93328
Liquid DAB + Substrate Chromogen System	DAKO	K3468
N-Acetyl-D-glucosamine	Sigma-Aldrich	A8625
NaCl (Sodium Chloride)	Sigma-Aldrich	S9625; CAS: 7647-14-5
N-Methyl-2-pyrrolidone (NMP)	Sigma-Aldrich	328634; CAS: 872-50-4
O.C.T Compound Sakura Finetek	Tissue-Tek	25608-930
Paraformaldehyde	Electron Microscopy Sciences	19202
PBS 10X (For IHC/IF)	ALAOS	PB515M-10
PBS w/o Ca^{2+}/ Mg^{2+} (For tissue culture)	Cultek S.L.U.	BE-17516F
Penicillin-Streptomycin	GIBCO; Life Technologies, S.A.	15070-063
Proteinase K	VWR International Eurolab, S.L	0706
Saline Sodium Citrate (SSC)	Sigma-Aldrich	S6639
Poly(ethylene glycol) 400 (PEG)	Sigma-Aldrich	202398; CAS: 25322-68-3

(*Continued on next page*)

Continued

REAGENT or RESOURCE	SOURCE	IDENTIFIER
Sulindac (99% purity)	Shanghai Moda Chemicals	CAS: 38194-50-2
Sunflower seed oil from *Helianthus annus*	Sigma-Aldrich	88921; CAS: 8001-21-6
TAE 50X (Tris-Acetic Acid-EDTA)	ALAOS	TA475M
Tamoxifen 400/CreER diet (400 mg/Kg)	Envigo	TD.130860
Torin 1	MedChem Express	HY-13003; CAS: 1222998-36-8
Triton X-100	Sigma-Aldrich	T8787; CAS: 9002-93-1
Tween 20	Sigma-Aldrich	P7949; CAS: 9005-64-5
Critical Commercial Assays		
Alcian Blue/PAS/Hematoxylin Stain Kit	DAKO	Cat#AR178
AmpONE Taq DNA polymerase	GeneAll	Cat#501-050
ATP Assay Kit (C/F)	BioVision	Cat#K354-100
Avidin/ Biotin Blocking Kit	Vector Laboratories	Cat#SP-2001
GoTaq qPCR Master Mix	Promega	Cat#A6002
Histology FISH Accessory Kit	DAKO	Cat#K5799
Kreatech Fluorescence in situ Hybridization (FISH)	Kreatech; Leica	N/A
Kreatech Tlk2 (11qE1) / Aurka (2qH3) Mouse FISH probes	Kreatech; Leica	KBI-30501
Lipofectamine RNA iMAX Transfection Reagent	Thermo Fisher	Cat#13778030
MiSeq Reagent Kit v2	Illumina	Cat#MS-102-2021
Oligonucleotide-based Sure Print G3 Mouse CGH Array Kit	Agilent Technologies	Cat#G4839; Design code: 27411
OxiSelect *In Vitro* ROS/RNS Assay Kit (Green fluorescence)	Cell Biolabs	Cat#STA-347
TruSeq Custom Amplicon Low Input Library Prep Kit	Illumina	Cat#FC-134-2001
Vectastain ABC HRP Kit (Peroxidase, Goat IgG)	Vector Laboratories	Cat#PK-4005
Vectastain ABC HRP Kit (Peroxidase, Mouse IgG)	Vector Laboratories	Cat#PK-4002
Vectastain ABC HRP Kit (Peroxidase, Rabbit IgG)	Vector Laboratories	Cat#PK-4001
Vectastain ABC HRP Kit (Peroxidase, Rat IgG)	Vector Laboratories	Cat#PK-4004
Deposited Data		
Apc sequencing data were deposited into the Sequence Read Archive	This paper	SRA: SRP126431 (BioProject number: PRJNA421772 and BioSample accession numbers SAMN08153392-SAMN08153418)
Experimental Models: Cell Lines		
Human: Colorectal carcinoma cell line: HCT-116 (gender: male)	ATCC	Cat#CCL-247; RRID: CVCL_0291
Mouse: Mouse embryonic fibroblasts: MEFs (gender: male)	Fawal et al., 2015	N/A
Experimental Models: Organisms/Strains		
Mouse: *Apc*(15lox): B6.129P2-Apctm1Rsmi/RfoJ	Dr. Ron Smits (Robanus-Maandag et al., 2010)	J:149225
Mouse: C57BL/6	CNIO Animal Facility	N/A
Mouse: CDK4-R24C/CDK6-R3IC	Dr. Marcos Malumbres (Rodriguez-Diez et al., 2014)	N/A
Mouse: FabplCre: Tg(Fabp1-cre)1Mmt	Dr. Ron Smits (Saam and Gordon, 1999)	J:59166
Mouse hMCRS1-tetON: ColA1_tethMCRS1	Dr. Nabil Djouder, Spanish National Cancer Research Center (CNIO)	This paper
Mouse: $MCRS1^{lox/lox}$: $Mcrs1^{tm1.1Ndj}$	Dr. Nabil Djouder (Fawal et al., 2015), Spanish National Cancer Research Center (CNIO)	J:232965

(*Continued on next page*)

Continued

REAGENT or RESOURCE	SOURCE	IDENTIFIER
Mouse: mTOR$^{lox/lox}$: B6.129S4-Mtor $^{tm1.2Koz}$/J	Dr. Sara Kozma (Risson et al., 2009)	J:011009
Mouse: p53 $^{lox/lox}$: B6.129P2-Trp53^{tm1Brn}/J	Spanish National Cancer Research Centre (CNIO)	J:61961
Mouse: RagA$^{lox/lox:}$ Rraga^{tm2Dmsa}	Dr. Alejo Efeyan (Efeyan et al., 2014)	J:213516
Mouse: Tg-UQ-CreERT2 : B6.Cg-Tg(UBC-cre/ERT2)1Ejb	CNIO Animal Facility	J:123200
Mouse: Villin-CreERT2 : Tg(Vil-cre/ERT2)23Syr	el Marjou et al., 2004	J:92295
Mouse: Villin-rtTA2-M2 mouse: Tg. B6. Villin-rtTA2-M2	Dr. Ron Smits (Roth et al., 2009), Erasmus MC; Universitaire Medisch Centrum Rotterdam	N/A
Oligonucleotides		
See Table S2 for genotyping	This paper	N/A
See Table S3 for qRT-PCR	This paper	N/A
Software and Algorithms		
Adobe Illustrator CS4	Adobe Design	http://creative.adobe.com/es/products/download/illustrator/
Agilent Genomic Workbench v7.0	Agilent Technologies	http://www.genomics.agilent.com/article.jsp?pageId=2167
Feature Extraction Software v10.7	Agilent Technologies	http://www.genomics.agilent.com/article.jsp?pageId=2059
Gitools 2.3.1	Gitools	http://www.gitools.org/
GraphPad Prism V5.0 software	GraphPad Software	https://www.graphpad.com/
Image J 1.7v software	NIH	https://imagej.nih.gov/ij/
Integrative Genomics Viewer (IGV)	Broad Institute	http://software.broadinstitute.org/software/igv/
Zytovision c.7.4 Image Analysis System	Applied Imaging, UK	http://zytovision.com/

CONTACT FOR REAGENT AND RESOURCE SHARING

Further information and requests for resources and reagents should be directed to and will be fulfilled by the Lead Contact, Nabil Djouder (ndjouder@cnio.es).

EXPERIMENTAL MODEL AND SUBJECT DETAILS

Mouse Models

MCRS1^{lox} allele was generated as previously described (Fawal et al., 2015). MCRS1^{Int} mice were obtained by crossing MCRS1$^{lox/lox}$ mice with Villin-CreERT2 mice (el Marjou et al., 2004). (MCRS1$^{(+/flox)Int}$) and homozygous (MCRS1$^{(flox/flox)Int}$) pups were born according to Mendelian ratio. A conditional knockin mouse model, expressing human MCRS1 (hMCRS1) in the intestine and colon epithelium after doxycycline administration was generated in our lab. Model was obtained by flippase-mediated targeting and recombination of inducible human *MCRS1* (hMCRS1) cDNA tagged with the Flag peptide in the 3′ untranslated region of the homing locus of the collagen type I, alpha 1 locus (*Col1a1)* gene in KH2 embryonic stem cells (ESCs), having a tetracycline operator (Tet-op). Proper recombination in the founder mouse was verified by Southern blot of the tail DNA as described previously (Beard et al., 2006). hMCRS1tetON mice were viable and born according to Mendelian ratio. Line was crossed with Villin-rtTA line kindly provided by Ron Smits (Roth et al., 2009) to overexpress MCRS1 specifically in the epithelium of the intestine. This strain will be referred to as hMCRS1-tetON^{Int}. *Apc*15lox (Robanus-Maandag et al., 2010) and FabplCre (Saam and Gordon, 1999) mice were kindly provided by Ron Smits. mTOR$^{lox/lox}$ mice were kindly obtained from Sara Kozma and crossed with Villin-CreERT2 mice to generate mTOR^{Int} mice (Risson et al., 2009). RagA$^{lox/lox}$ mice were provided by Alejo Efeyan (Efeyan et al., 2014). CDK4-R24C/CDK6-R31C mutant mice were obtained from Marcos Malumbres (Rodriguez-Diez et al., 2014). p53$^{lox/lox}$ mice were obtained from E. Wagner's lab. All mice have been housed in pathogen-free conditions, with a 12 hr light/dark cycle between 8:00 and 20:00 in a temperature-controlled room (22°C ± 1°C). Mice were backcrossed to C57BL/6 for at least six generations. All experiments were approved by the CNIO-ISCIII Ethics Committee and performed in accordance with the guidelines for ethical conduct in the care and use of animals as stated in the international guiding principles for biomedical research involving animals, developed by the Council for International

Organizations of Medical Sciences. Littermates were always used as controls. Males and females were used for the study. No gender differences were observed and age/developmental stage of mice is included appropriately in the text and Figure Legends. Food (Harlan Laboratories and Research Diets Inc.) and water were provided *ad libitum.*

Intestine Preparation

Small intestine and colon were removed from mice, flushed with 10% formalin and incubated in 10% formalin for 5 min. Subsequently, intestines were opened longitudinally, 'swiss-rolled', incubated overnight in 10% formalin at room temperature and processed for paraffin embedding.

Tumor Quantification

Intestine and colon were opened longitudinally and macroscopic visible polyps were counted. Histopathological scoring of tumors was performed based on H&E staining of colon paraffin-embedded section according to reported guidelines (Boivin et al., 2003). Normal mucosa or hyperplastic regions were scored as grade 0, GIN was scored as grade 1, low grade adenoma was scored as grade 2, high grade adenoma was scored as grade 3 and adenocarcinoma as grade 4.

Human Samples

Human CRC samples were obtained from the CNIO Biobank and human UC and CD samples were obtained and processed at the University Guadalajara Hospital. Human samples were approved by the appropriate ethic committee and informed consent was obtained from all subjects.

Cell Culture

Culture of HCT-116 Cells

HCT-116 are colorectal carcinoma cells derived from an adult male human. Cells were cultured in high-glucose DMEM supplemented with glutamine, 10% FBS and 100 units/ml penicillin and 0.1 mg/ml streptomycin and maintained at 37° in a humidified atmosphere of 5% CO_2. Cells were subculture when 80%-90% of confluence was reached as previously reported (Fawal et al., 2015).

Culture of MEFs

Mouse embryonic fibrolasts (MEFs) (Fawal et al., 2015) derived from male embryo were cultured in DMEM supplemented with 10% FCS, 100 units/ml penicillin and 0.1 mg/ml streptomycin, and maintained at 37° in a humidified atmosphere of 5% CO_2. Transfection was performed using Lipofectamine RNAiMAX following manufacturer's instructions and as previously reported (Fawal et al., 2015). Cells were plated on a 6-well plate, treated with either siRNA-Ctr (control) or siRNA-MCRS1 (Dharmacon), and analyzed 72 hr after the transfection. For deforolimus treatment cells were treated with 0.2 nM deforolimus dissolved in DMSO and analyzed 72 hr later. MEFs were treated with 10 μM tamoxifen and 250 nM (Bioron) dNTPs supplemented every 12 hr for 72 hr.

METHOD DETAILS

Mouse Diets and Treatments

Cre-mediated recombinase was activated by feeding mice with tamoxifen diet at the concentration of 400 mg/kg at 8 weeks of age and for the next 2 days or weeks. Villin-rtTA2 mediated human MCRS1 (hMCRS1) expression was activated by feeding mice continuously with doxycycline diet at concentration of 50 mg/kg since weaning.

Irradiation was performed with the use of lethal (14 Gy) dose. Mice were analyzed 72 hr after irradiation.

For FITC-dextran permeability assay mice were first starved for 12 h and then given 60 mg/100 g of body weight of FITC-dextran dissolved in water (Sigma-Aldrich) by oral gavages. Serum was collected 4 hr later and analyzed by spectrofluorometry at the 485 nm excitation wavelength and 528 nm emission wavelength.

AOM/DSS treatment was performed as previously described (Neufert et al., 2007). Briefly, at 10 weeks of age mice were injected intraperitoneally with 7.5 mg/kg AOM (Sigma-Aldrich) and treated with 2% DSS (30- 50 kDa, colitis grade, MP Biomedicals) in drinking water for 5 days. DSS treatment was repeated 3 times once per 4 weeks. Mice were sacrificed 100 or 200 days after AOM injection. For the experiments with deletion after tumor formation, mice were fed for 2 weeks with tamoxifen diet at the concentration of 400 mg/kg starting 100 days after initial carcinogen injection.

Acute DSS treatment was performed as previously described (Chassaing et al., 2014). Briefly, at 10 weeks of age mice were treated with 2% DSS in drinking water for 5 days. Afterwards mice were transferred to drinking water and sacrificed 2 to 4 days later.

For Bromodeoxyuridine (BrdU) pulse mice were injected with 1 mg/mouse of BrdU (Sigma-Aldrich) in PBS and sacrificed 2 hr later.

Isocaloric protein free diet was obtained from Envigo (# TD.93328). Mice were treated with the diet for 2 weeks prior irradiation to 14 Gy.

Sulindac (99% purity, Shanghai Moda Chemicals Co., Ltd) was dissolved in drinking water at the concentration of 0.18 g/L, and given to 8-week-old mice for 100 days or 20 weeks. Sulindac was changed every second day, freshly prepared and filtered.

Deforolimus (MedChem Express) was dissolved in 1% DMSO in sunflower seed oil and injected to 8-week-old mice at the concentration of 20 mg/kg every day for 2 weeks or every second day for 100 days. 1% DMSO in sunflower seed oil was injected as placebo.

Torin 1 (MedChem Express) was dissolved in NMP/PEG 400 (1:4) and injected to 8-week-old mice in the final concentration of 10 mg/kg every second day for 2 weeks. NMP/PEG 400 (1:4) was injected as placebo.

Anti-mouse IL-6 antibody (BioXCell), clone MP5-20F3 was diluted in sterile PBS and injected to 8-week-old mice every second day at the concentration of 200 μg/mouse for 100 days. Control mice were injected with rat IgG1 (BioXCell), clone HRPN.

Anti mouse IL-6R antibody, clone MR16-1 (kindly provided by Tadamitsu Kishimoto and Chugai Pharmaceutical Co., Ltd.) (Okazaki et al., 2002) was diluted in sterile PBS and injected to 8-week-old mice every second day at the concentration of 200 μg/mouse for 100 days or 20 weeks. Rat IgG1 (BioXCell), clone HRPN was used as a control.

100% hydrolyzed hydropure whey protein extract (Amix) was dissolved in drinking water at the concentration of 2% and given to 10-week old mice for 100 days or for 5 days in combination with 2% DSS. Whey protein extract was changed every second day, freshly prepared and autoclaved. Whey protein was enriched in essential amino acids (glutamine = 17.3 g/100 g of pure protein) and branched chain amino acids (leucine = 10.4 g/100 g of pure protein). Of note, chow diet (normal diet) has 2.9 g/100g of glutamine and 1.4 g/100g of leucine.

Fluorescence *In Situ* Hybridization

Fluorescence in situ Hybridization (FISH) chromosome enumeration probes specifically recognizing 11qE1 and 2qH3 cytobands of mouse chromosomes were purchased from Kreatech (Leica). FISH was performed as previously described (Rodriguez-Perales et al., 2016) on 5mm paraffined tissue sections mounted on positively charged slides (SuperFrost, Thermo Scientific). The slides were first deparaffined in xylene and rehydrated gradually in a series of ethanol. The Histology FISH Accessory Kit (DAKO) was used following the manufacturer's instructions. Briefly, the method consists of pre-treatment in 2-[N-morpholino]ethanesulphonic acid (MES), followed by a protein digestion performed in pepsin solution. After dehydratation, the samples were denatured in the presence of the specific probe at 66°C for 10 min and left overnight for hybridization at 45°C in a DAKO hybridizer machine. Finally, the slides were washed with 20×SSC (saline-sodium citrate) buffer with detergent Tween-20 at 63°C, and mounted in fluorescence mounting medium (DAPI). FISH signals were manually enumerated within nuclei all over the tissue. FISH images were also captured using a CCD camera (Photometrics SenSys camera) connected to a PC running the Zytovision image analysis system (Applied Imaging Ltd., UK) with focus motor and Z stack software.

CIN Analysis

The CIN score (CS) is a metric devised to quantify the alterations (gains or losses) detected in a sample. It is calculated for the two probes combined for each nuclei analyzed. To assess CIN score aneuploidies of chromosomes 11 and 2 were evaluated. Samples were FISH hybridized with specific chromosomes 11 and 2 probes, cells were manually evaluated and Z-stack images were acquired. 100 nuclei were evaluated from each sample. Due to the mathematical negating properties of averaging aneuploidies (gains) in chromosome numbers within a given sample, a CS was devised, which was calculated for each individual chromosome and two chromosomes combined (CS_C). In essence, a CS is a metric used to describe the aneuploidies in chromosome numbers within a given sample, so that comparisons can be made between samples. For reference purposes, $CS_C = 0$ indicates that the nucleus is diploid (i.e., harbors two copies of each chromosome), while $CS_C > 0$ identifies increases in gains and losses of chromosome(s). In addition, an overall mean CS can be calculated for a given sample by averaging the individual CS values for that condition. The formula used to calculate the score is the following: $CS=1/n \sum[(e_{11}-o_{11})+(e_2-o_2)]$, where CS calculate the value obtained when the observed (o) number of a given signal is subtracted from the expected (e) number of the two signals of a wild type cell [58]. A Table S1 is included with the raw data obtained by FISH.

aCGH Analysis

aCGH analysis was used to evaluate the number of putative chromosomal breaks underlying gene amplification and deletion events. aCGH analysis was conducted on oligonucleotide-based SurePrint G3 Mouse CGH Array Kit 4×180K microarray slides (Design Code: 27411) that has a backbone resolution of ~150Kb (Agilent Technologies, Santa Clara, CA, USA). Sample DNAs were labeled with Cy5 dye and reference DNA sample was labeled with Cy3 dye. Hybridizations were performed according to the manufacturer's protocols. Arrays were scanned using the G2565BA DNA Microarray Scanner (Agilent Technologies), and their data were extracted using the Feature Extraction Software v10.7 (Agilent Technologies).

The Aberration Detection Method 2 (ADM- 2) algorithm of Genomic Workbench (Agilent Tech) was used to identify contiguous genomic regions that correspond to chromosomal aberrations or copy number variations. Signal fluorescent intensities of each probe from both samples are considered to be proportional to the amount of respective genomic sequence present. For each probe, there exists a log ratio and the raw measurements of red and green intensity ratios. The ADM-2 interprets log ratios and probe quality measures from the microarray to identify all aberrant intervals in a given sample with consistently high or low log ratios based on a statistical score. The log ratio of signal is obtained from comparing each channel for each probe and converting the ratio to log base 2. The ADM- 2 algorithm searches for regions that are statistically different from a log ratio score expected value of zero, or no change, between channels. The CNV regions were scored based on the average quality weighted log ratio of the sample and reference channels exceeds a 6-value threshold. In the aCGH analysis, intervals with scores greater than the value of 6 were marked significant and retained as aberrant regions. All intervals found in this process were reported, and a plot was generated. The intervals are rendered as steps in the visualization panel. The height of each step is equal to the average log ratio of that interval.

Immunohistochemistry and Histology

Immunohistochemistry of paraffin-embedded sections was performed as previously described (Tummala et al., 2014). Freshly harvested murine intestines and colons were fixed immediately in 10% buffered formalin solution overnight and embedded in paraffin. Tissue sections of 3 μm were deparafinized, rehydrated, and antigen retrived by using 1 M sodium citrate buffer (pH 6.5). After blocking endogenous peroxidase using 3% H_2O_2 for 10 min, and permeabilized in 0.2% Triton X-100 in PBS for 10 min, sections were blocked for 1 hr at room temperature with 5% of serum diluted in PBS with 0.2% Triton X-100. Furthermore, sections were incubated with primary antibodies overnight at 4°C. Vectastain ABC kit (Vector Laboratories, Inc) was used, following manufacturer's instructions. Sections were then incubated with 33-diaminobenzidinetetracloride (DAB) (Dako) and counterstained with hematoxylin. Alcian blue/PAS staining was performed using Dako Alcian Blue/PAS/Hematoxylin Stain Kit (#AR178) according to the manufacturer's instructions.

Senescence-Associated β-Galactosidase Assay

Intestine was removed from mice, washed with cold PBS, opened longitudinally and directly embedded and frozen in O.C.T compound (Tissue-Tek). 10 μm sections of frozen tissue were fixed in 0.5% glutaraldehyde/PBS for 10 min and washed for 3 min in buffer containing: PBS pH 5.5, 1 mM $MgCl_2$, 50 mM imidazole and 20 mM N-acetyloglucosamine. Afterwards, slides were incubated overnight in 37 °C in staining solution containing: 1 mg/ml 5-bromo-4-chloro-3-indolyl-β-D-galactopyranoside (Apollo Scientific) in dimethylformamide, 40 mM citric acid/sodium phosphatate pH 6, 5 mM potassium ferricyanide, 5 mM potassium ferrocyanide, 150 mM NaCl, 2 mM $MgCl_2$, 50 mM imidazole, 20 mM N-acetyloglucosamine. Next, slides were washed 3 times with PBS, counterstained with eosin and mounted in 70% glycerol.

Immunoblotting

Small intestine and colon were removed from mice; proximal ileum and distal colon were flushed with cold PBS, opened longitudinally and directly frozen in liquid nitrogen. Immunoblotting was performed as previously reported (Tummala et al., 2014). 50 to 100 mg of frozen tissues were lysed using RIPA lysis buffer containing: 10 mM Tris pH 8.0, 100 mM NaCl, 1 mM EDTA, 1mM EGTA, 2 mM Na_3VO_4, 20 mM $Na_4P_2O_7$, 1 mM NaF, 0.5% sodium deoxycholate, 0.1% SDS, 1% Triton-X 100, 10% glycerol, and supplemented with 10 mg/ml protease inhibitor aprotinin and 1 mM PMSF. Lysates were homogenized using Precellys 24 Bead Mill homogenizer (Bertin Technologies) (15 x 2 s, 5500 w) and then clarified by centrifugation at 4 °C and 10.000 g for 10 min. Protein concentration was measured using Bio-Rad Bradford reagent (Bio-Rad) and bovine serum albumin (BSA) as standard protein. 1 mg/ml concentrated lysates were made by boiling the appropriate amount of protein lysates with 2x laemmli buffer (4% SDS, 20% glycerol, 10% β-mercaptoethanol, 0.004% bromophenol blue in 0.2 M Tris-HCL of pH 7) at 70 °C, for 10 min. 10-30 μg of protein lysates were subjected into SDS-PAGE gels, and transferred to nitrocellulose membranes. The membranes were blocked with 5% nonfat milk in Tris-buffered saline containing 1% Tween-20 for 1 hr at room temperature. Blots were immune-stained with the indicated antibodies. Immunoblots were processed by ECL (Amersham) according to the manufacturer's instructions.

Serum Cytokine Measurement

Blood was obtained by cardiac puncture into EDTA containing tubes (Aquisel) and centrifuged 20 min, 4000 g to obtain serum. IL-6, IL-12, TNFα, IL-23 concentrations were determined using corresponding CBA flex set beads according to manufacturer's instructions.

ROS, ATP and mtDNA Measurement

ROS measurement was performed using OxiSelect In Vitro ROS/RNS Assay Kit (Green fluorescence) (Cell Biolabs, # STA-347) following the manufacturer's instruction. ATP measurement was performed using ATP Assay Kit (C/F) (BioVision, # K354-100) following the manufacturer's instruction. mtDNA content was measured using qRT-PCR as previously described (Cunningham et al., 2007).

Apc Gene Sequencing

Mouse *Apc* coding sequence library was synthesized using TruSeq Custom Amplicon Low Input Library Prep (Illumina) and sequenced with MiSeq System (Illumina) combined with the MiSeq Reagent Kit v2 (500 cycles) (500 to 15000 reads per sample) (Illumina). Analysis of the variants was performed using Intergative Genomics Viewer and heat map was obtained using Gitools. *Apc* sequencing data were deposited into the Sequence Read Archive under the accession number SRA: SRP126431.

Genotyping and qRT-PCR

For genotyping, DNA was extracted by overnight incubation of fingers with 500 μl of the cell lysis buffer (1% SDS, 0.1 M NaCl, 0.1 M EDTA, 0.05 M Tris (pH 8) and 400 μg/ml of proteinase K). DNA obtained after saturated salt precipitation was further precipitated using ice-cold isopropanol. DNA pellet was washed with 70% ethanol. Purified DNA was dried and resuspended in 200 μl of distilled water. 1 μl of DNA was used for genotyping. Primers used for genotyping are listed in Table S2.

For qRT-PCR, was performed as previously described (Tummala et al., 2014). Total RNA was extracted from frozen small intestine or colon, using Trizol (Sigma). First strand cDNA synthesis was performed using an ABI PRISM 7700 (Life Technologies), and GoTaq Real-Time qPCR mix (Promega). Fold changes were determined by using $2^{\Delta\Delta}$CT and normalized to *Actb* (β-actin). Finally, the fold

changes were obtained by converting the logarithmic scale to an exponential scale ($2^{\Delta\Delta}$CT). qRT-PCR primers are listed in Table S3.

QUANTIFICATION AND STATISTICAL ANALYSIS

Image Analysis

Ten images per slide were taken at 10 X magnifications and quantified using color de-convolution, a colocalization finder and image analysis tools available in Image J 1.7v software. For IHC quantification, at least 50 crypts or villi were analyzed for each independent experiment. For FISH analysis at least 100 nuclei were analyzed for each independent experiment.

Statistical Analysis

Statistical analyses were performed using GraphPad Prism V5.0 software. Statistical significance (p) ($p \leq 0.05$ = *, $p \leq 0.01$ = ** and $p \leq 0.001$ = ***) between the means of a minimum of three groups was determined using unpaired two-tailed Student's t test or linear regression analysis. Results are expressed as the mean value ± Standard Error of the Mean (SEM). "n" represents number of mice or cells used in each experiments, as indicated in Figure Legends. All results including western blot are representative of at least three independent experiments.

DATA AND SOFTWARE AVAILABILITY

Apc sequencing data were deposited into the Sequence Read Archive under the number SRA: SRP126431.